Experimental Mechanics (2022) 62:1437–1459
https://doi.org/10.1007/s11340-022-00843-9

SP ISS: ADVANCES IN RESIDUAL STRESS TECHNOLOGY

The Effect of Bulk Residual Stress on Milling-Induced Residual Stress and Distortion

C. R. Chighizola[1] · C. R. D'Elia[1] · J. E. Jonsson[1] · D. Weber[2] · B. Kirsch[2] · J. C. Aurich[2] · B. S. Linke[1] · M. R. Hill[1]

Received: 21 January 2022 / Accepted: 22 March 2022 / Published online: 21 April 2022

Abstract

Background Distortion arises during machining of metallic parts from two main mechanisms: 1) release of bulk residual stress (BRS) in the pre-form, and 2) permanent deformation induced by cut tools. Interaction between these mechanisms is unexplored.

Objective Assess this interaction using aluminum samples that have a flat surface with variations of BRS, where that surface is subsequently milled, and we observe milling-induced residual stress (MIRS) and distortion.

Methods Plate samples are cut from two kinds of large blocks, one kind stress-relieved by stretching and a second kind solution heat treated, quenched and aged. The BRS field in the plates is known from a recent series of measurements, being small in the stress relieved plates (within ±20 MPa) and large (±100 MPa) in the quenched plates, varying from tension to compression over the surface that is milled. MIRS is measured following milling using hole-drilling. Distortions of thin wafers cut at the milled surfaces are used to elucidate BRS/MIRS interactions. A finite element (FE) model and a strength of materials model are each used to assess consistency between wafer distortion and measured MIRS.

Results Milling in samples with high BRS magnitude changes the directions of MIRS and distortion relative to the milling direction, with the direction of maximum curvature rotating toward or away from the milling direction depending on the sign and direction of BRS. High magnitude BRS was also found to increase the wafer peak arc height, nearly doubling the amount found in low BRS samples.

Conclusion Measured residual stress and observed wafer distortion both show interactions between MIRS and BRS. Stress analysis models show that the differences in measured MIRS are consistent with the differences in observed distortion.

Keywords Machining distortion · Residual stress · Milling · Quenching · Manufacturing

Introduction

Thin-walled lightweight components are widely used to increase in-service performance by reducing weight. These components are often made of high strength aluminum alloy due to its high specific strength and good manufacturability. A shortcoming of these components is their increased likelihood to distort due to low stiffness and residual stresses [1]. The combination of solution heat treatment and quenching in aluminum alloys can lead to significant bulk residual stress (BRS) that increases the likelihood for distortion during material removal by machining [2, 3]. Distortion is also caused by milling induced residual stress (MIRS) [4]. These two types of residual stress have different character, BRS having longer length scale (on the order of the thickness of raw stock), and MIRS being limited to a thin layer at the milled surface [3, 5].

The literature shows that distortion in thin-walled parts correlates to MIRS left in parts after machining and the amount of BRS released in material removed. Madariaga et al. [4] investigated the correlation of MIRS and part distortion using finite element (FE) models and distortion experiments. Model inputs were developed from measurements of MIRS made using fine increment hole-drilling. It was found that the influence of MIRS on final part distortion

✉ M. R. Hill
mrhill@ucdavis.edu

[1] Department of Mechanical and Aerospace Engineering, University of California, One Shields Avenue, Davis, CA 95616, US

[2] Institute for Manufacturing Technology and Production Systems, TU Kaiserslautern, Erwin-Schrödinger-Straße 52, 67663 Kaiserslautern, Germany

depends on the sign, magnitude, and position of the MIRS layer with respect to the neutral axis of the part. Madariaga et al. reported that BRS (measured using the contour method [6]) and MIRS (measured with hole-drilling) both affect the final distortion, with increases in MIRS magnitude corresponding to increases in distortion. Their model accurately predicted distortion. Work by Zhang et al. [7] investigated the correlation between distortion and MIRS in experiments using 7050-T7451. They reported that the magnitude of distortion is attributable to BRS relaxation and MIRS. Material removal creates an imbalance of BRS and the MIRS layer also creates an imbalance, and these imbalances increase distortion. Zhang et al. used finite element models to validate distortion measurements, where the models took as inputs residual stress data from slitting measurements. The model results were identical in shape to the measured distortions but differed in magnitude. Similar work by Masoudi et al. [3] studied the correlation between MIRS and distortion in thin-walled samples in stress relieved 7050-T651. They reported increased distortion when there were increases in magnitude and depth of MIRS. As in the work by Zhang et al. [7], Masoudi et al. reported that greater imbalance of MIRS lead to greater distortion.

These previous efforts show that both BRS and MIRS contribute to the distortion of thin-walled parts. The shape and magnitude of distortion is linked to the magnitude and spatial distributions of BRS and MIRS. The earlier studies have used stress relieved materials, which are mostly free of BRS. No attention has been given to how BRS might affect MIRS, and how the interaction might influence distortion in thin-walled parts. This paper investigates the interaction between MIRS and BRS in milling of aluminum. This is accomplished by developing a set of samples having different BRS, milling them, making measurements of MIRS by fine-increment hole-drilling, performing distortion experiments, and performing correlative analysis.

Methods

Material and geometry

The material used in this study is AA7050-T7451, a common aerospace aluminum alloy whose temper designation indicates a rolled plate artificially over-aged (T74) and stretched for stress relief (TXX51). The material was purchased as a plate 1250 mm long (along the rolling direction, L) by 1250 mm wide (along the long transverse, LT) by 102 mm thick (ST). Six blocks measuring 660 mm (L) by 206 mm (LT) by 102 mm thick (ST) were removed from this parent stock. Blocks A, B, and C were used as supplied, but blocks D, F, and G were heat treated to T74 condition. The heat treatment follows industry specification [8] where the plate is solution heat treated to 475 °C, quenched in water to room temperature, then aged in two stages, at 107 °C for 6 to 8 hours and then 163 °C for 24 to 30 hours. Quenching in water from 475 °C is known to induce a high BRS. Subsequently, each of the T7451 and T74 blocks were cut using a plate saw into fifteen plate-shaped samples, each plate 206 mm long (LT) by 102 mm wide (ST) by 28 mm thick (L) (see Fig. 1). A material coordinate system is chosen such that the x-direction is along the 206 mm plate length, the y-direction is along the 102 mm width, and the z-direction is along the 28 mm thickness.

Milling conditions

Several stress relieved (T7451) and quenched (T74) plates are uniformly face milled on one of the 206 mm by 102 mm faces. The milling tool is a three-flute, 12 mm Kennametal F3AA1200AWL end mill, which represents a typical end mill used in high-speed machining of aerospace grade aluminum alloys like AA7050. The milling is performed using a cutting speed of 200 mm/min and a feed per tooth of

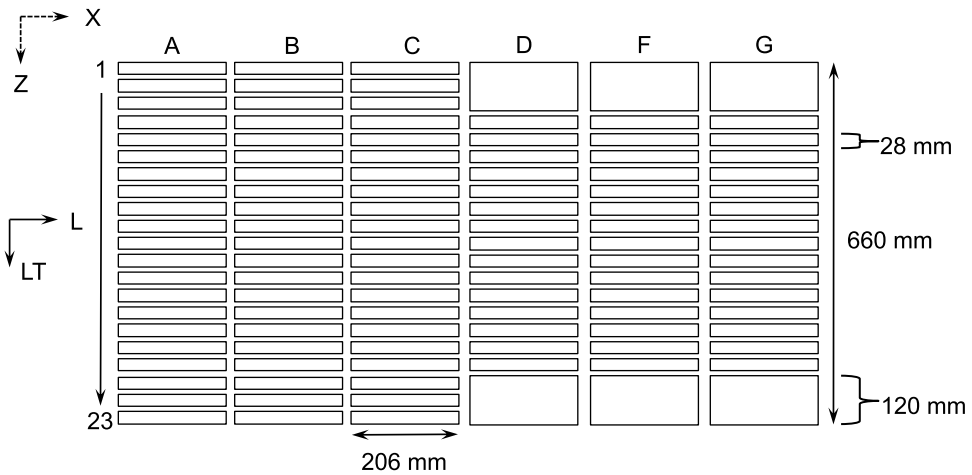

Fig. 1 Diagrams of the sample labeling scheme and locations of samples where the longitudinal rolling direction (L) is along x and the long transverse direction (LT) is along z [11]. The 120 mm sections of material are cut away and discarded to remove quench end effects. Individual samples are coded as L#, where L is A, B, C, D, E, or G, indicating the parent block, and # indicates the position of the sample in the block (positions 1 to 23 for blocks A, B, and C; positions 1 to 15 for blocks D, F and G)

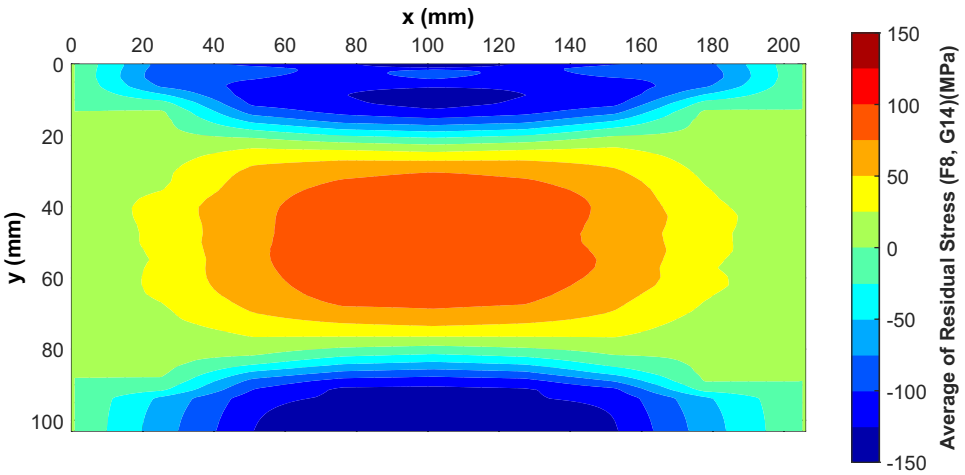

Fig. 2 Color map of bulk residual stress along the plate length (σ_{xx}) measured using CMOD slitting approach [11]

0.2 mm, which have been shown in prior work to produce a significant layer of MIRS in stress relieved material [9]. The axial and radial engagement lengths were fixed at 3 and 4 mm respectively, so milling reduces the plate thickness from 28 mm to 25 mm. All milling is performed on a DMG Mori DMU 70 CNC with uniform down milling and without coolant (dry milling). A random order of milling the samples was chosen to minimize the influence of the tool wear. The tool wear was monitored after milling each sample by a macroscope, so that worn tools were exchanged if wear in the form of corner break outs was detected qualitatively [10].

Summary of BRS

To support the investigation of the interaction between of BRS and MIRS, it is necessary to measure the BRS fields in the quenched plate-like samples. This was accomplished for the present samples in recent work where BRS was measured using a cut mouth opening displacement (CMOD) variation of slitting [11]. The results show that the quenched plates have a paraboloid spatial distribution of residual normal stress components, and the residual stress levels are a significant fraction (50 to 80%) of material strength. As seen in Figs. 2 and 3 the BRS field has significant directionality. Near the plate center, for example, the stress state is nearly uniaxial tension with stress along x (Fig. 2) much larger than stress along y (Fig. 3); near the upper and lower plate boundaries (y near 0 or 102 mm) the stress is nearly uniaxial compression (stress along x compressive and stress along y near zero). Because of this BRS directionality, milling along x or milling along y allows observation of different interactions between the milling process and the underlying BRS field. Milling was therefore performed in some samples at 0°, where the milling direction (α) is along negative x from 206 to 0 mm and the step over direction (β) is along negative y from 102 to 0 mm. In other samples milling was performed at 90°, where α is along y from 0 to 102 mm and β is along negative x from 206 to 0 mm (see Fig. 4). Examination of MIRS and distortion in the milling coordinate system is useful in assessing the effects of BRS (and its directionality).

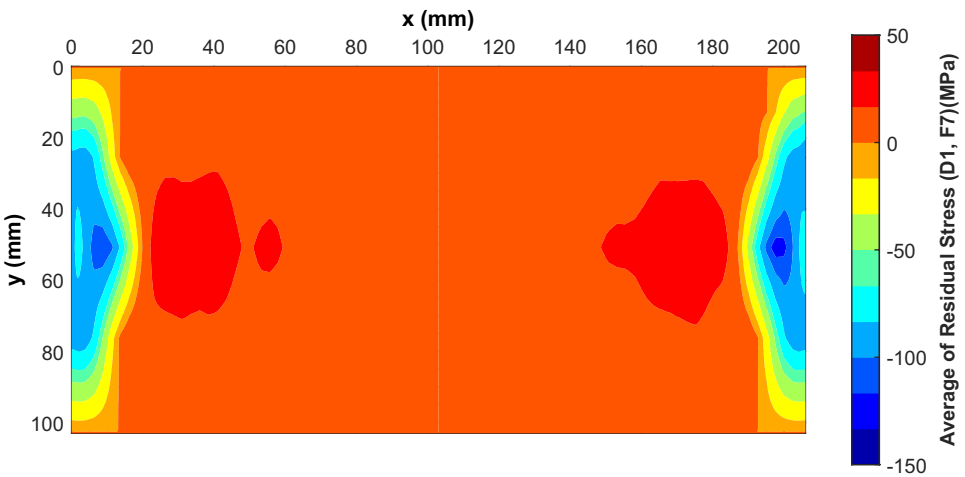

Fig. 3 Color map of bulk residual stress along the plate width (σ_{yy}) measured using CMOD slitting approach [11]

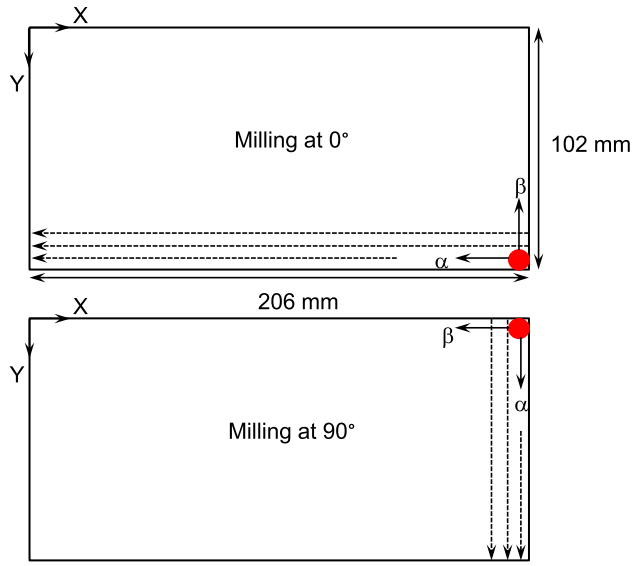

Fig. 4 Diagrams of the two milling directions where coordinates X and Y represent the material reference frame and coordinates α and β represent the milling reference frame with α along the tool travel and β along the step over

Wafer distortion experiments

The influence of BRS on distortion is shown using a post-milling distortion experiment first shown in our earlier work [5]. A cube of material having side length 25 mm is removed from the machined samples by wire electric discharge machining (EDM). The cube is rotated 90° about the y-axis and a thin wafer of thickness t_w = 1 mm, including the machined surface, is cut from the cube by wire EDM (see Fig. 5). The distorted shape of the wafer is expected to be analogous to the MIRS, as described in [5]. The form of the wire EDM wafer surface is determined using a laser profilometer at a set of points with 0.2 mm spacing along both the 25 mm width and 25 mm length of the surface. The surface form data are post processed (trimmed, leveled, and offset) to provide consistent comparisons among wafers. The surface form data are trimmed to remove extraneous data points. The trimmed data are leveled by fitting the data to a plane and subtracting the fit plane from the data. The trimmed and leveled surface form data are then offset to place the center of the wafer surface at zero height (i.e., z = 0). To quantify the influence of BRS on MIRS the wafer distortion experiment is performed in stress-relieved samples and in quenched samples. The effects of BRS directionality are assessed by removing cubes from different regions having compressive, near zero, or tensile BRS. Multiple wafers are removed in a single stress-relieved sample to highlight repeatability of the wafer distortion experiment.

Milling-induced residual stress measurements

To understand the influence of typical milling and measurement variations from sample to sample it is useful to perform multiple measurements of MIRS in replicate stress-relieved samples. Computing the average and standard deviation of repeated measurements in replicate samples defines the typical MIRS field and its expected variation, which can then be compared to MIRS found in quenched plates. Our prior work [5] shows that for the above milling parameters MIRS in stress-relieved samples comprises a layer of compressive stress from the surface to depths of 0.2 mm having a maximum compressive stress of -150 to -180 MPa at a depth of roughly 0.05 mm. MIRS is measured using the hole-drilling technique, following the ASTM standard [12] but using fine cut depth increments [13]. Hole-drilling was shown to have useful repeatability for MIRS in aluminum [5]. Hole-drilling also provides three components of residual stress versus depth in a single measurement, which is necessary to assess distortion [5]. The hole-drilling technique involves application of a three-element strain gage rosette and the cutting of a hole (2 mm in diameter) in increments of depth. At each increment of hole depth, three strains are recorded. Stress versus depth is computed from strain versus depth data by solving an inverse problem [12]. Hole depths used are shown in Table 1,

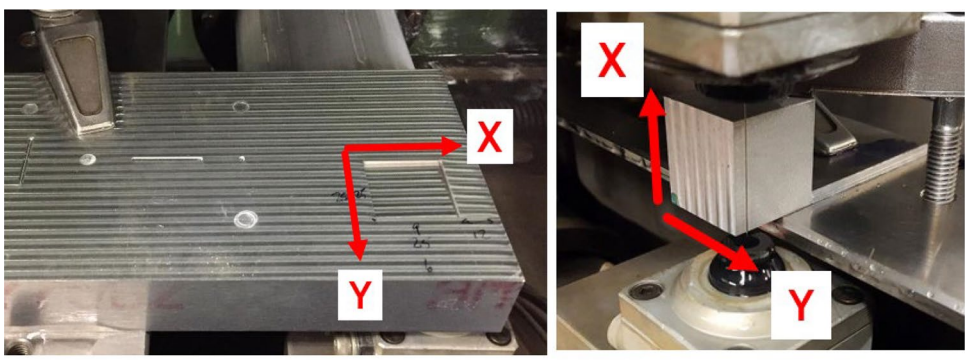

a b

Fig. 5 Wafer experiment setup to (**a**) remove the 25 by 25 by 25 mm cube and (**b**) remove the 1 mm thick wafer [5]

comprising 10 depth increments of 0.0127 mm, 6 depth increments of 0.0254 mm, and 6 depth increments of 0.0508 mm, to a total depth of 0.584 mm (see Table 1). As in the prior work [5], a depth correction is used to offset intended hole depths to match the measured final cut depth, which provides more consistent results by accounting for the potential offset between the workpiece and the mill used to perform hole-drilling.

Summary of experiments

For both the stress-relieved and quenched samples measurements are made away from the plate edges and at various locations. For quenched sample D3 milled at 0°, MIRS is measured at locations where the BRS along α is compressive ($\sigma_{\alpha\alpha} < 0$), near zero ($\sigma_{\alpha\alpha} \approx 0$), and tensile ($\sigma_{\alpha\alpha} > 0$) (reference Fig. 2). For quenched sample D12 milled at 90°, MIRS is measured at a location where the BRS along β is tensile ($\sigma_{\beta\beta} > 0$). A total of 21 hole-drilling measurements are made on both stress-relieved and quenched samples. In stress-relieved samples A20, B4, A18 and B20, a total of 15 measurements are made (3 for A20, 6 for B4, 3 for A18, and 3 for B20). In quenched sample D3 milled at 0° a total of 5 measurements are made with 1 in compressive BRS, 1 in near zero BRS, and 3 in tensile BRS. In high stress sample D12 milled at 90°, 1 measurement is made in an area of tensile BRS. These measurements are located at the coordinates given in Table 2 which also shows the BRS state indicated by the prior CMOD slitting measurements (shown graphically in Figs. 2 and 3). All measurements are located very precisely relative to the milling passes, with the hole center at a ridge left between passes (evident in Fig. 5 and detailed more clearly in our prior work [5]).

A total of 12 wafer distortion measurements are made in both stress-relieved and quenched samples. In stress-relieved samples A20, B20, and B4 a total of 7 wafers are removed (3 for A20, 3 for B20, and 1 for B4) at the locations shown in Table 3. No wafer was removed in sample A18. In high stress sample D3 milled at 0°, a total of 3 wafers are removed, one each where the BRS along α is compressive, near zero, and tensile, as shown in Table 3. In high stress sample D12 milled at 0°, 2 wafers are removed, one in an area where the BRS along β is tensile, and another where the BRS along β is compressive. When possible, wafers are removed at locations where hole-drilling measurements were made previously, with the hole-drilling sites located at the center of the wafer. For locations where the two measurements cannot be superposed, the wafers are removed as close as possible to hole-drilling locations. It is expected that the 2 mm diameter hole from hole-drilling will not alter significantly the overall MIRS-induced distortion of the 25 mm wafer.

Table 1 Summary of material removal schedule used with the hole-drilling technique for assessing both MIRS and BRS in milled samples

Increment mm	Depth mm
0	-
0.0127	0.0127
0.0127	0.0254
0.0127	0.0381
0.0127	0.0508
0.0127	0.0635
0.0127	0.0762
0.0127	0.0889
0.0127	0.1016
0.0127	0.1143
0.0127	0.127
0.0254	0.1524
0.0254	0.1778
0.0254	0.2032
0.0254	0.2286
0.0254	0.254
0.0254	0.2794
0.0508	0.3302
0.0508	0.381
0.0508	0.4318
0.0508	0.4826
0.0508	0.5334
0.0508	0.5842

Data assessment using elastic stress analysis

Companion models allow wafer distortion to be predicted from measured MIRS. Two types of models are used, a finite element (FE) model and a strength of materials (SoM) analysis. The FE model uses measured MIRS depth profile data as an input and provides wafer distortion as an output. For samples with multiple MIRS measurements, the average depth profile is used as the input. The FE model domain reflects that of the wafer geometry in the experiment and uses brick elements with uniform in-plane size of 0.50 mm. There are 20 elements through the 1 mm wafer thickness with size of 0.01 mm at the machined surface and increasing to a size of 0.14 mm at the EDM surface (see Fig. 6). The material is assumed linear elastic with elastic properties $E = 71$ GPa and $\upsilon = 0.33$. Boundary conditions necessary to suppress rigid body motion are applied. Models are made for the conditions of Table 3. The MIRS for each condition is linearly interpolated at element centroids of the FE model and imposed as an initial stress; MIRS at the maximum depth measured by hole-drilling (0.584 mm, Table 1) is used for element centroids at deeper depths. Equilibrium is then determined in the FE solver [14], and computed displacements are reported,

Table 2 Summary of hole-drilling measurement locations in samples with low and high stress states

Sample	Milling Direction (degrees)	Locations (x, y) (mm, mm)	CMOD Bulk Residual Stress State
A20	0	(103, 24) (103, 78) (182, 50)	Near zero (stress-relieved)
B4	0	(50, 24) (103, 24) (103, 50) (153, 24) (153, 50) (153, 78)	Near zero (stress-relieved)
A18	0	(103, 24) (103, 50) (103, 78)	Near zero (stress-relieved)
B20	90	(103, 36) (103, 78) (128, 50)	Near zero (stress-relieved)
D3	0	(103, 15) (25, 50) (128, 50), (103, 50), (78, 50)	Compressive Near zero Tensile
D12	90	(128, 50)	Tensile

which comprise the estimated distortion. The FE model displacement outputs are post-processed using the same steps that are used for the wafer topography measurements and then the computed and observed topography are compared. Similarity between FE model outputs and observed topography would indicate consistency between measured MIRS and observed wafer distortion.

Table 3 Wafer removal locations (center of wafer) and BRS from CMOD slitting

Sample	Milling Direction (degrees)	Location (X, Y) (mm, mm)	BRS (MPa)
A20	0	(24, 64) (182, 64) (182, 36)	$\sigma_{\alpha\alpha}$ = 10.0 $\sigma_{\beta\beta}$ = -0.3
B4	0	(24, 64)	$\sigma_{\alpha\alpha}$ = 10.0 $\sigma_{\beta\beta}$ = -0.3
A18	0	-	-
B20	90	(24, 64) (182, 64) (182, 36)	$\sigma_{\alpha\alpha}$ = -0.3 $\sigma_{\beta\beta}$ = 10.0
D3	0	(25, 50) (103, 15) (128, 50)	$\sigma_{\alpha\alpha}$ = 32.8 $\sigma_{\beta\beta}$ = 31.3 $\sigma_{\alpha\alpha}$ = -101.2 $\sigma_{\beta\beta}$ = 0 $\sigma_{\alpha\alpha}$ = 85.8 $\sigma_{\beta\beta}$ = 13.3
D12	90	(128, 50) (103,87)	$\sigma_{\alpha\alpha}$ = 13.3 $\sigma_{\beta\beta}$ = 85.8 $\sigma_{\alpha\alpha}$ = 0 $\sigma_{\beta\beta}$ = -91.2

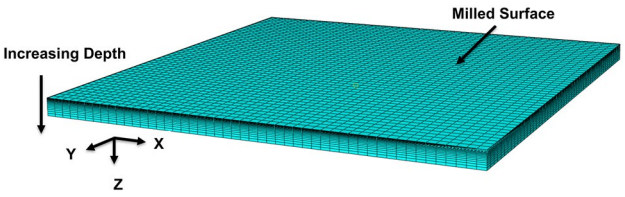

Fig. 6 Finite element mesh used in the wafer distortion model [5]

Wafer distortion is also determined from MIRS using strength of materials (SoM) theory. The SoM analysis uses hole-drilling stress versus depth profiles as input (see Fig. 7). The computation begins by defining a bulk stress, σ_b, for each stress component as the average of MIRS residual stress over all depths between 0.2 to 0.5 mm (i.e., far from the surface where MIRS is expected to be negligible). An effective stress, σ_e, for each stress component is then determined as the measured MIRS minus σ_b (the subtraction due to the fact that a wafer with uniform bulk stress should be expected to exhibit no measurable curvature (distortion)). The depth of the layer of non-zero effective stress, called the effective depth, d_e, is determined using linear interpolation of the hole-drilling data with depths > 0.05 mm to find the depth where σ_e crosses 0 MPa (data at shallow depths < 0.05 mm are excluded due to potential for near-zero stress very close to the milled surface, as shown in prior work [5]). The data, σ_e and d_e, reflect an effective stress area (see Fig. 7). Integration of the effective stress area for the ij component of measured stress provides a force,

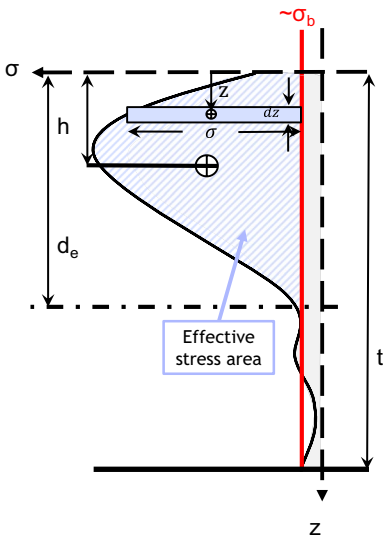

Fig. 7 Diagram depicting parameters in the strength of material elastic stress analysis model using MIRS hole-drilling data

$$F_{ij} = \int_0^{d_{e,ij}} \sigma_{e,ij} dA \tag{1}$$

and a distance from the machined surface to the location of the centroid of the effective stress area,

$$h_{ij} = \frac{\int_0^{d_{e,ij}} \sigma_{e,ij} z dA}{F_{ij}} \tag{2}$$

as shown in Fig. 7. For a planar analysis the differential area $dA = Bdz$ and B is taken as unity (1 mm). The centroidal distances for different stress components are typically close to one another, so an average centroidal distance is useful in further analysis,

$$h = \frac{1}{3}\left(h_{xx} + h_{yy} + h_{xy}\right). \tag{3}$$

A layer-average stress for the ij component of stress is then computed using F_{ij}, h_{ij}, and h

$$\tilde{\sigma}_{ij} = \frac{F_{ij}}{2Bh_{ij}}\left(\frac{h_{ij}}{h}\right). \tag{4}$$

The layer-average stress components are used to compute layer average principal stresses ($\tilde{\sigma}_1$ and $\tilde{\sigma}_2$) and principal angle (θ_1) using typical stress transformation equations. As typical, $\tilde{\sigma}_1$ is the most positive principal stress, and θ_1 is the angle to that stress. Since MIRS in aluminum is expected to be compressive [5], the maximum distortion should be due to $\tilde{\sigma}_2$ and to occur along the angle $\theta_2 = \theta_1 + 90°$. Forces and bending moments along principal directions are computed using the layer average principal stresses and the average depth,

$$\overline{F}_1 = \tilde{\sigma}_1 \cdot 2hB \tag{5}$$

$$\overline{F}_2 = \tilde{\sigma}_2 \cdot 2hB \tag{6}$$

$$\overline{M}_1 = \overline{F}_1\left(\frac{t_w}{2} - h\right) \tag{7}$$

$$\overline{M}_2 = \overline{F}_2\left(\frac{t_w}{2} - h\right) \tag{8}$$

where $t_w = 1$ mm is the wafer thickness in the distortion experiment and $B = 1$ mm is an arbitrary out-of-plane thickness. (Note: the subscript notation here is consistent with historical descriptions of plate bending theory, where $\overline{M}_1$ is the bending moment causing curvature along θ_1; this notation is different than often used in vector mechanics where a force along θ_1 would cause a bending moment vector along θ_2.) From these forces and moments, the radius of curvature is computed using strength of materials (plate bending) theory

$$R_2 = -\frac{EBt_w{}^3}{12\left(\overline{M}_2 - \upsilon\overline{M}_1\right)} \tag{9}$$

with values of E and $\upsilon = 0.3$ provided above.

Correlation between distortion, MIRS, and BRS

To assess the correlation between MIRS influenced by BRS and distortion it is useful to assess a common set of parameters derived from each of the three types of data (experiment, FE model, and SoM model). The prior work in stress-relieved material showed that wafer distortion of milled surfaces are convex and roughly ellipsoidal [5]. The highest curvature is rotated relative to the machining axes by an angle referred to as the clocking angle, θ_c, where the angle is measured from the α direction and positive toward β. This angle is a useful distortion metric. A second useful metric is an arc height along this orientation, S_c. For the SoM model, $\theta_c = \theta_2$ and S_c is computed from $R_c = R_2$ using the geometry of a circular sector, as explained below. For the experiment and FE model, surface distortion data near the wafer centroid are trimmed to within a radius, $r_t = 10$ mm. A rectangle of length $2r_t$ and width $0.15r_t$ is used to mask the topography data, where the rectangle is centered on the wafer and the 20 mm length is aligned at an angle θ from the milling direction α. A univariate parabola is fit to the masked data using least squares, and a radius of curvature R(θ) of the fit determined at the wafer center. This calculation is repeated for angles θ = 0°, 0.5°, 1°, …, 180° and a minimum value of R(θ) is determined, which provides the clocking angle θ_c and the minimum radius of curvature R_c for data from the experiment and the FE model.

For the experiment and the two (SoM and FE) models, the arc height S_c along θ_c over a distance $2r_t$ is computed from R_c using the geometry of a circular sector [15]

$$S_c = R_c - \sqrt{R_c{}^2 - r_t{}^2}. \tag{10}$$

Comparisons of S_c and θ_c (as determined from SoM, FE, and measured distortion) for wafers removed at locations of varying BRS show how MIRS and BRS interact.

Results

Wafer distortion

Figure 8 shows observed distortion for multiple wafers removed from stress-relieved sample B20 (milled at 90°, $\sigma_{\alpha\alpha} \approx \sigma_{\beta\beta} \approx 0$ MPa). The topography shows that the milled surface becomes convex when the wafers are cut free. The observed distortion appears very similar for each wafer,

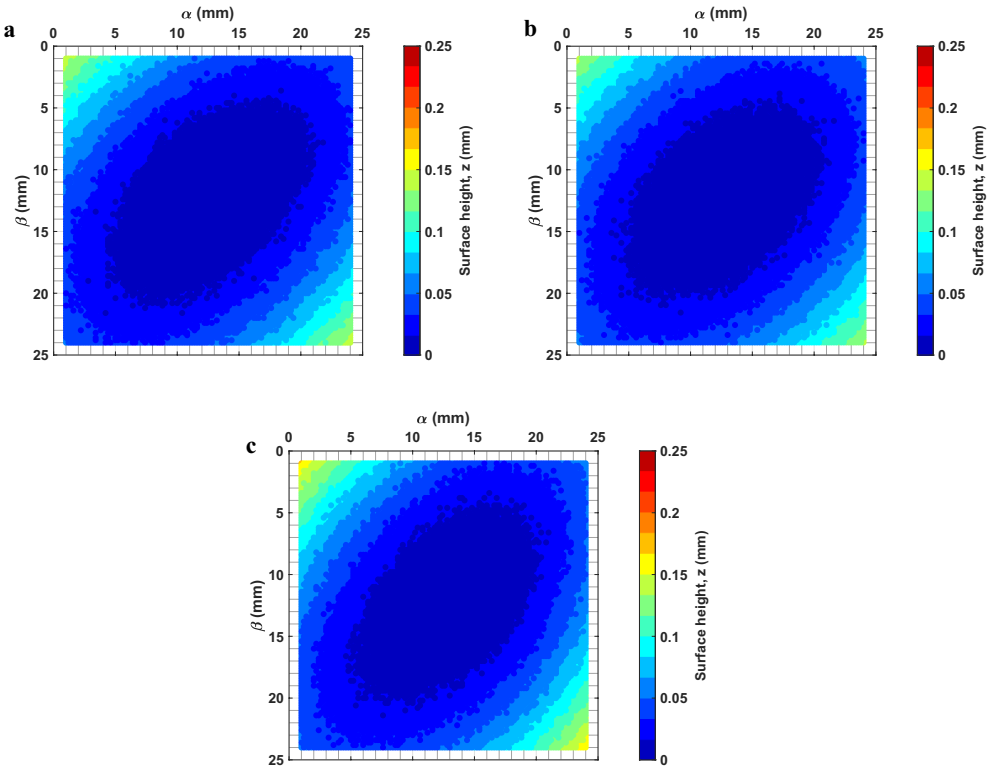

Fig. 8 Comparison of observed distortion in sample B20 for wafers removed at various locations: (**a**) (24, 64) mm, (**b**) (182, 64) mm, and (**c**) (182,36) mm

with similar peak to valley distortion (about 0.15 mm) and similar clocking angle θ_c near 45°. The good agreement among measurements in Fig. 8 shows that the wafer distortion experiment is repeatable.

The left column of Fig. 9 shows observed distortion of wafers removed from stress-relieved samples A20 (Fig. 9(a)) milled at 0° and B20 (Fig. 9(c)) milled at 90°; the figure also shows a wafer from quenched sample D3 milled at 0°, removed in an area where BRS is near zero (Fig. 9(e)). Note that the in-plane coordinate axes are relative to the milling directions, α and β. Distortion for A20 and B20 reflect the average topography of the 3 different wafers removed from each sample. The observed distortion is similar among these wafers, exhibiting similar peak to valley distortion (0.15 mm for A20 and B20, and 0.20 mm for D3) and similar clocking angle (48° for A20, 45° for B20, and 51° for D3). Overall, the similarity in distortion magnitude and clocking angle suggest the distortion is not sensitive to changes in milling direction (0° or 90°) or the stress level of the sample, at locations where the underlying BRS is near zero.

The left column of Fig. 10 shows observed distortion in wafers cut from quenched samples D3 (milled at 0°) and D12 (milled at 90°). (Note: again, the coordinate axes are relative to the milling directions, α and β). Wafers are removed from sample D3 at locations where the BRS in the α-direction (x-direction) is compressive (Fig. 10(a)) or tensile (Fig. 10(c)). The wafers from sample D12 are removed where BRS in the β-direction (x-direction) is tensile (Fig. 10(e)) or compressive (Fig. 10(g)). The figure shows, at the lower and right side of the axes, the levels of bulk residual stress σ_b found from hole-drilling in each direction at each location (except for Fig. 10(g), where the BRS shown comes from CMOD slitting because hole-drilling data were not available at that location). For sample D3, the observed peak distortion of the wafer removed in compressive BRS (0.175 mm, Fig. 10(a)) is less than that of the wafer removed in tensile BRS (0.25 mm, Fig. 10(c)). The clocking angles differ significantly, being 81° and 24° for D3 in compressive and tensile BRS respectively. Comparison of samples D3 and D12 in tensile BRS shows that they exhibit very similar peak distortion (0.23 to 0.25 mm) but significantly different clocking angles (24° and 75°, Fig. 10(c, e) respectively). Comparison of samples D3 and D12 in compressive BRS shows that they exhibit similar peak to distortion (0.15 to 0.18 mm) but significantly different clocking angles (80° and 13.5°, Fig. 10(a, g), respectively). Overall, the direction and magnitude of the underlying BRS field relative to the milling direction has a significant effect on observed wafer distortion.

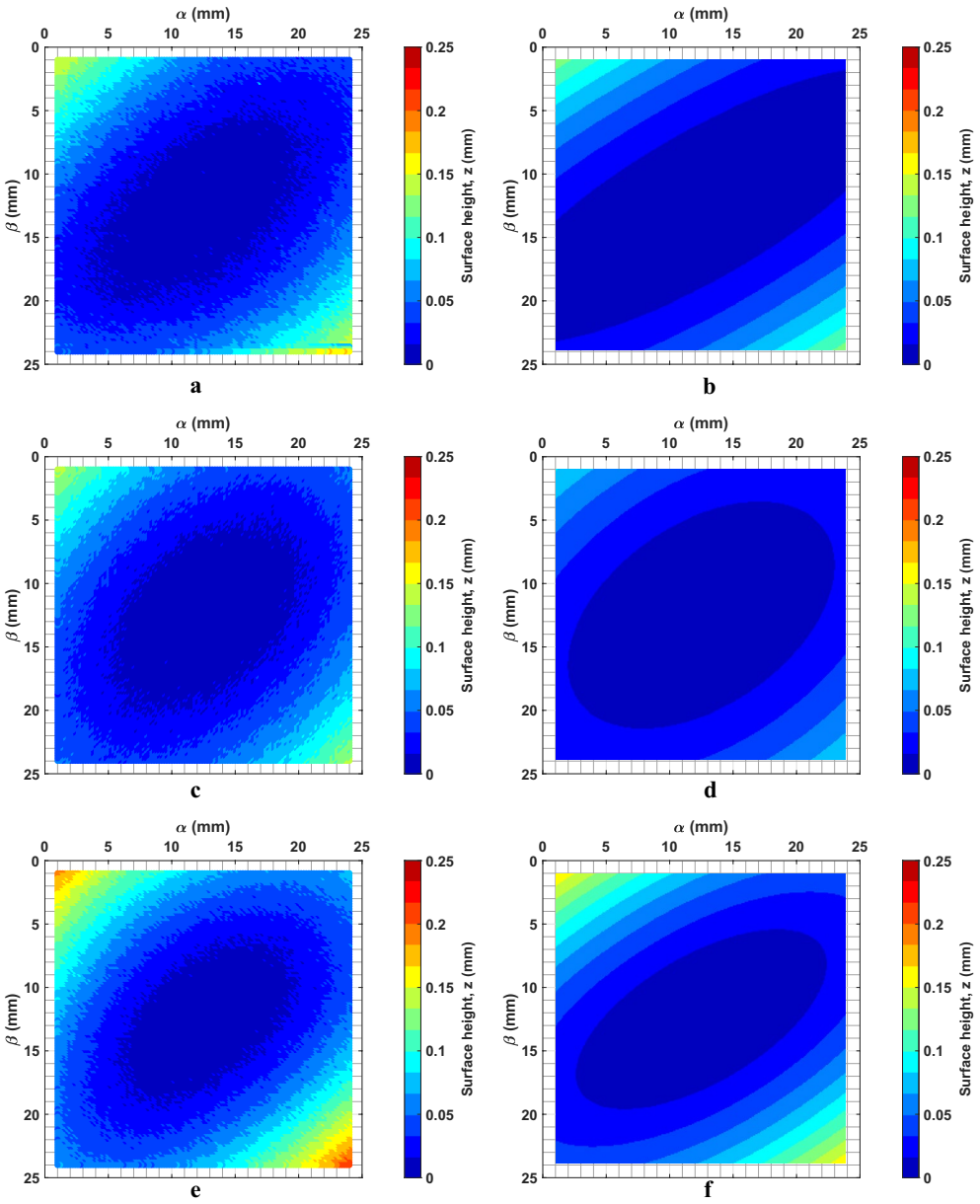

Fig. 9 Comparison of observed distortion (left column) and distortion computed using FE model (right column) in stress-relieved samples (**a, b**) A20 (milled at 0°), (**c, d**) B20 (milled at 90°), and quenched sample (**e, f**) D3 (milled at 0°) at locations of near zero BRS

MIRS measurements

Figure 11 shows repeated measurements of the three components of MIRS in stress-relieved sample A20 milled at 0°. A square root (-$\sqrt{}$-) shape in stress is typical of MIRS in aluminum, as is the return to 0 MPa at depth of about 0.20 mm (Fig. 11(a–c)). The multiple measurements exhibit consistency in magnitude and depth of stress with the milling direction component ($\sigma_{\alpha\alpha}$) maximum being -100±10 MPa at 0.055 mm, the transverse ($\sigma_{\beta\beta}$) maximum being -120±10 MPa at 0.06 mm, and the shear ($\sigma_{\alpha\beta}$) maximum being -50 MPa. The representative three-sample average stress versus depth profile of Fig. 11(d) shows $\sigma_{\beta\beta}$ somewhat larger than $\sigma_{\alpha\alpha}$ (maximum values -120 and -100 MPa, respectively) and about 0.050 mm deeper. The shear stress $\sigma_{\alpha\beta}$ is smaller than the normal stresses, at -50 MPa. The depth of maximum stress is consistent between $\sigma_{\alpha\alpha}$ and $\sigma_{\beta\beta}$, being 0.06 mm, with the depth of maximum shear stress $\sigma_{\alpha\beta}$ being shallower at 0.04 mm. Error bars in Fig. 11(d) represent the standard deviation of stress at each depth. Each stress component shows greater scatter near the surface, which reflects effects of surface texture and the inherent

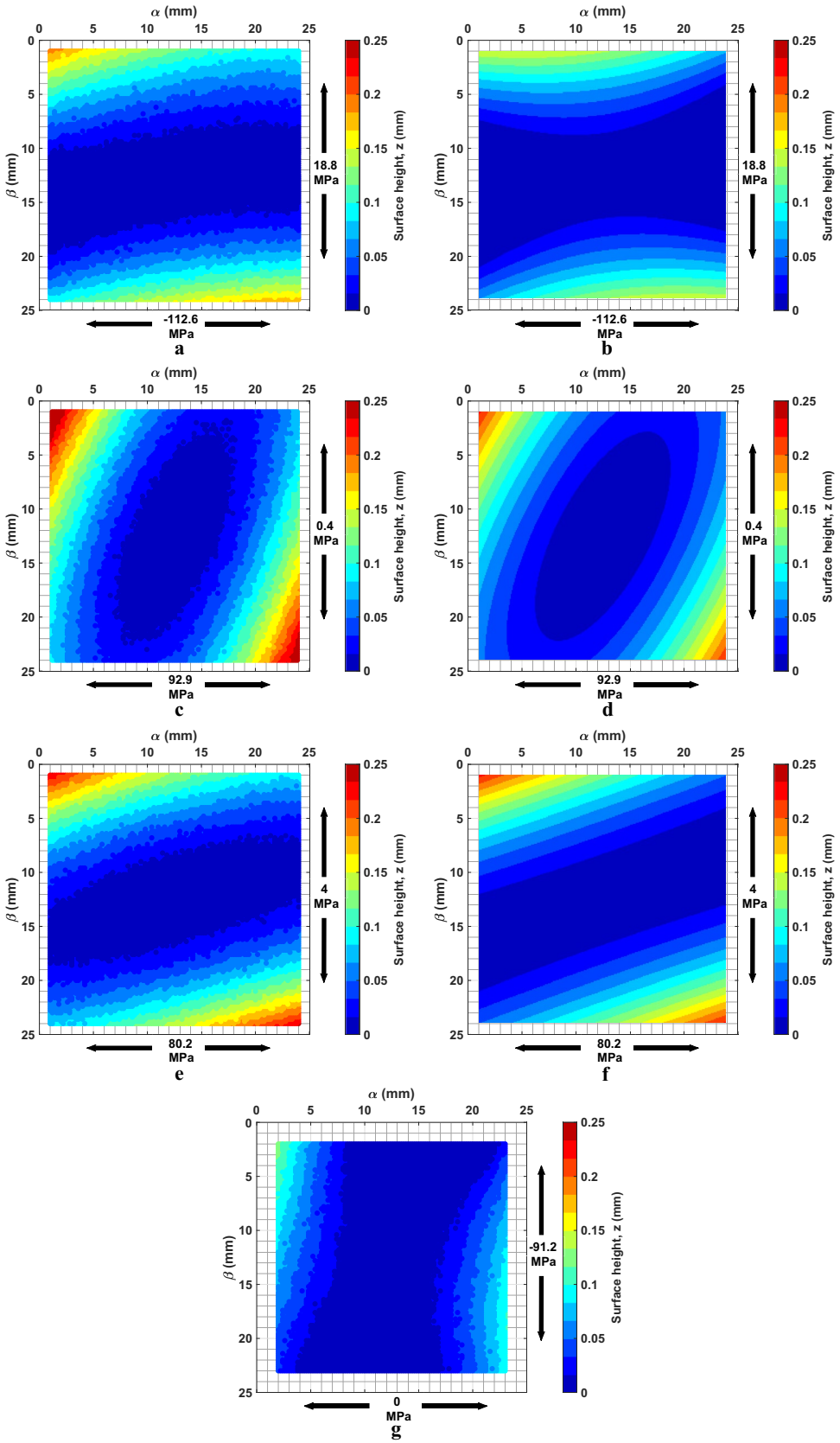

Fig. 10 Comparison of observed distortion (left column) and distortion computed using FE model (right column) in quenched samples (**a, b**) D3 (milled at 0°) in compressive BRS, (**c, d**) D3 (milled at 0°) in tensile BRS, (**e, f**) D12 (milled at 90°) in tensile BRS, and (**g**) D12 (milled at 90°) in compressive BRS (values of BRS along α and β are indicated by labels along the axes)

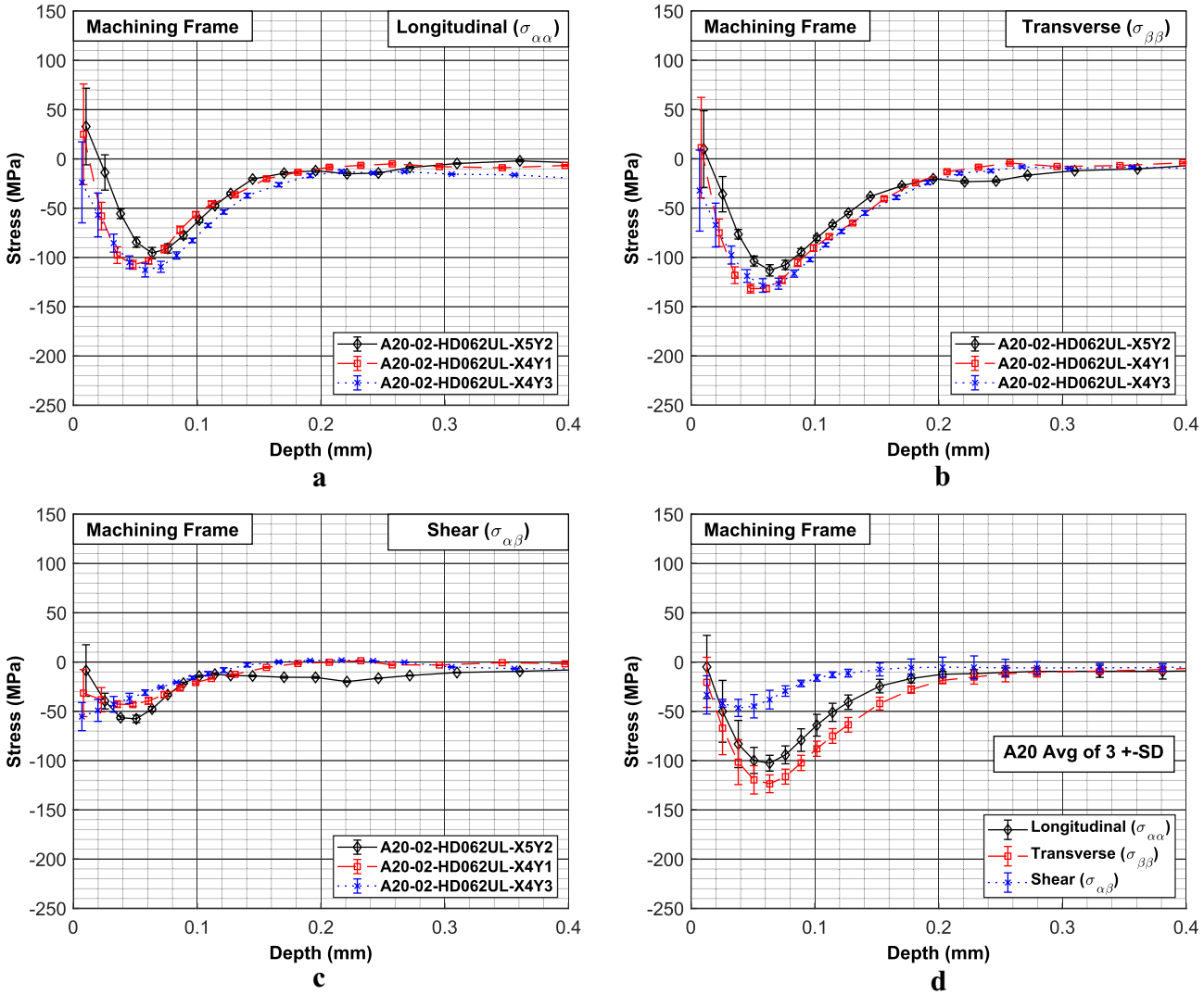

Fig. 11 Replicate MIRS data on sample A20 for (**a**) longitudinal, (**b**) transverse, (**c**) shear stress and (**d**) the representative (average) stress versus depth profiles

uncertainty of the hole-drilling technique at very shallow depths [5].

To assess sample to sample repeatability of MIRS, three or six hole-drilling measurements were made in each of three stress-relieved samples milled at 0°. Figure 12 shows three components of MIRS for samples B4, A20, and A18. The plot reports the average depth profile for six repeated measurements in B4 and three repeated measurements each in A20 and B20. All samples exhibit similar trends but with some significant differences. Longitudinal stress data ($\sigma_{\alpha\alpha}$, Fig. 12(a)) show B4 and A18 having similar maximum compressive stress (-150 MPa) at a similar depth (0.045 mm), but data for A20 show a lower stress (-100 MPa) at a deeper depth (0.06 mm). Transverse stress ($\sigma_{\beta\beta}$, Fig. 12(b)) data show that B4 and A18 have similar depth of maximum stress (0.045 mm) but different magnitude (-165 MPa for B4 and -120 MPa for A18). Data for A20 show a deeper peak stress (0.060 mm) and a magnitude similar to that in A18 (-120 MPa). Shear stress ($\sigma_{\alpha\beta}$, Fig. 12(c)) data show a consistent stress versus depth profile for all three samples. The grand average stress versus depth profiles in Fig. 12(d), computed from data on all three samples, show maximum compressive $\sigma_{\alpha\alpha}$ and $\sigma_{\beta\beta}$ to be similar in magnitude (-135 MPa) and to occur at a similar depth (0.05 mm). The two standard deviation error bars of Fig. 12(d) cover the range of the single sample average depth profiles. The grand average depth profiles (and two-standard-deviation bounds) are useful in judging subsequent measurements because they comprise

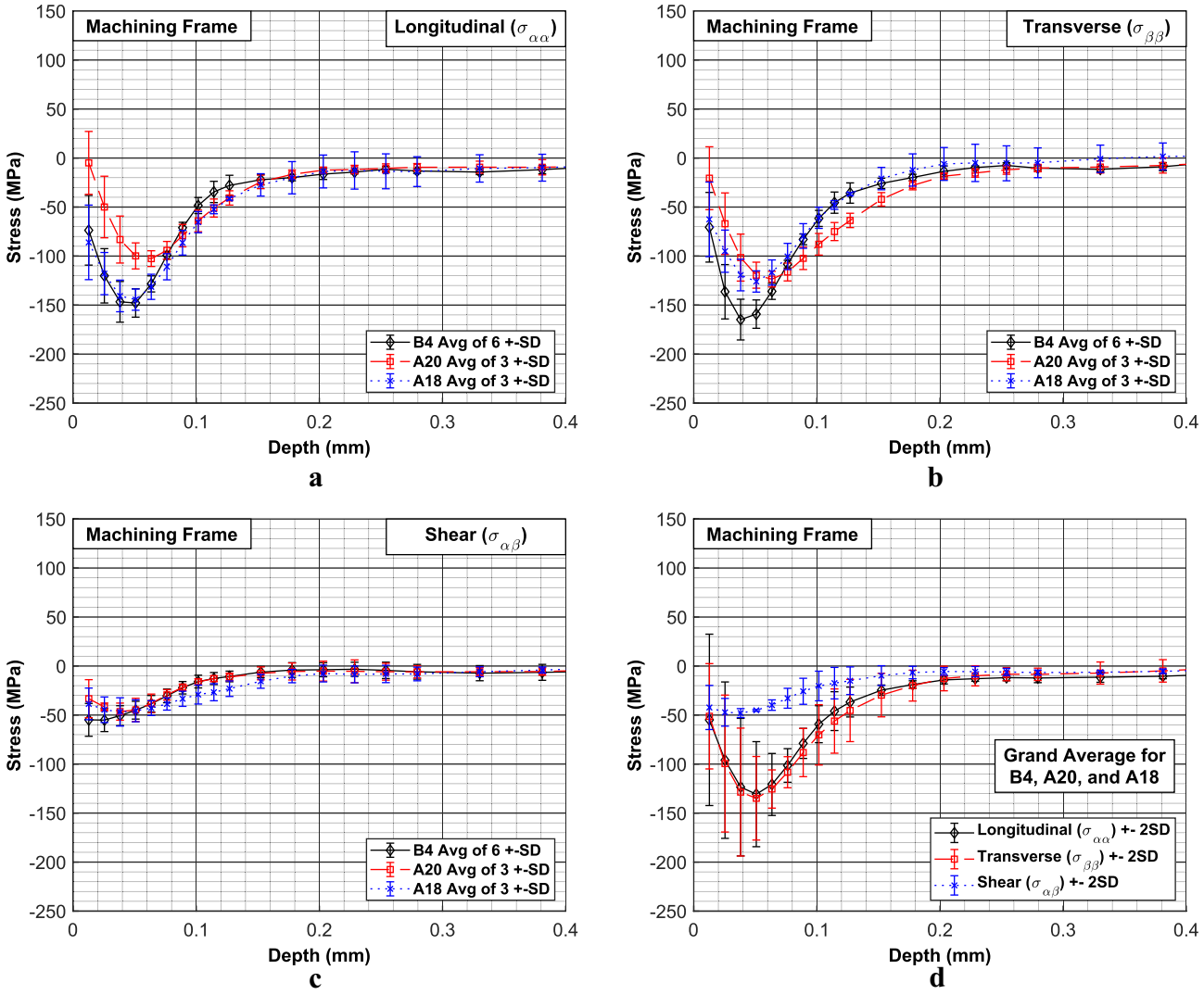

Fig. 12 Comparison of representative MIRS profiles for stress-relieved samples machined identically (B4, A20, A18) (**a**) longitudinal, (**b**) transverse, (**c**) shear stress and (**d**) the grand average stress versus depth profiles

observations by repeated measurements on replicate samples milled identically and, as such, include the influences of variations typical in milling and in MIRS measurements.

Figure 13 shows repeated measurements of MIRS in low stress sample B20 milled at 90°. These data exhibit somewhat high scatter near the surface compared to those for sample A20 (Fig. 11) but share similar trends. The three-measurement average stress profiles of Fig. 13(d) are quite consistent with the grand average for 0° milling of Fig. 12(d). Compared with 0° milling (Fig. 12(d)), the normal stress data for 90° milling (Fig. 13d) have a slightly shallower depth of peak compressive stress (0.040 mm for 90° versus 0.050 mm for 0°) and a faster return to zero stress (e.g., stress at a depth of 0.1 mm is -30 to -40 MPa for 90° versus -50 to -70 MPa for 0°). The largest difference is that shear stress for 90° milling is significantly lower and shallower than that for 0° milling. Therefore, we conclude that 0° and 90° milling create similar but somewhat different MIRS.

Figure 14 shows repeated measurements of MIRS in a region of tensile BRS in the α-direction (x-direction) in sample D3 comprised of three stress components (Fig. 14(a) thru Fig. 14(c)) and the average stress profiles (Fig. 14(d)). The tensile BRS in the α-direction (90 to 100 MPa) is clearly indicated in the $\sigma_{\alpha\alpha}$ data at depths > 0.25 mm (Fig. 14(a, d)). A square root (-$\sqrt{}$-) shape in normal stress components is evident and is consistent across multiple measurements for both components. Compared to MIRS found in stress-relieved material (Fig. 12), the near surface (< 0.05 mm) stress set up in tensile BRS (Fig. 14) is quite similar, with somewhat larger shear stress. For $\sigma_{\alpha\alpha}$, the near-surface

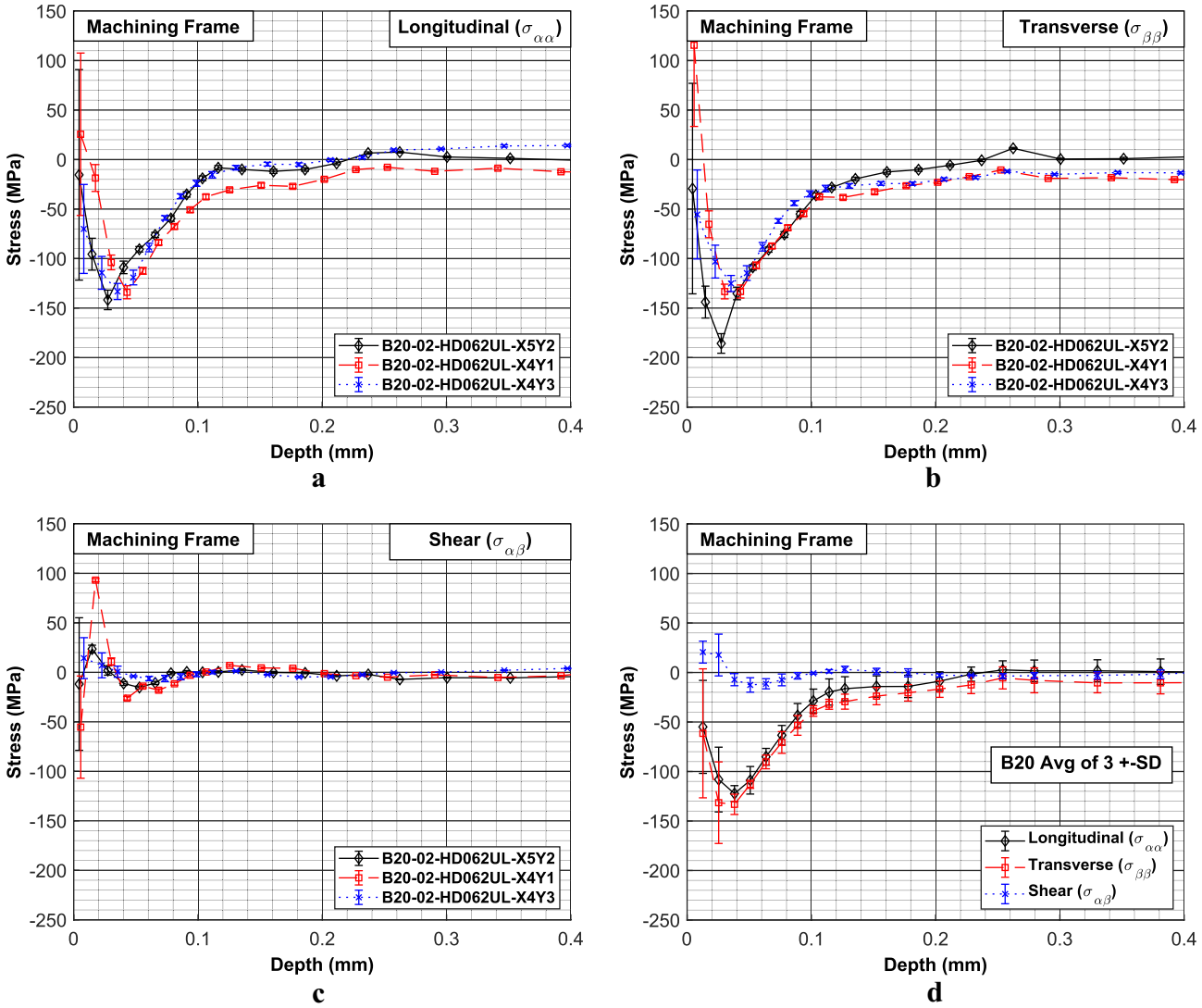

Fig. 13 Replicate MIRS data on sample B20 machined at 90° for (**a**) longitudinal, (**b**) transverse, (**c**) shear stress and (**d**) the representative (average) stress versus depth profiles

compression and subsurface tension lead to a much larger stress gradient at intermediate depths (0.05 to 0.2 mm) than found for stress relieved material.

Figure 15 shows three components of MIRS in sample D3 (milled at 0°) made at locations of compressive, near zero, and tensile BRS along α. The measurements in tensile BRS are the averaged profiles of Fig. 14(d). At deep depths (≈ 0.3 mm), the differences in BRS are evident, and the BRS is essentially uniaxial along the 0° milling direction. The maximum compressive values of near surface normal stress ($\sigma_{\alpha\alpha}$ and $\sigma_{\beta\beta}$) decrease with decreasing BRS, while the maximum magnitude of shear stress ($\sigma_{\alpha\beta}$) increases. The depths of maximum compression decrease slightly with increasing BRS for $\sigma_{\alpha\alpha}$, and are invariant for $\sigma_{\beta\beta}$ and $\sigma_{\alpha\beta}$. Overall, there is a systematic influence of BRS on MIRS.

Figure 16 compares the measured MIRS set up in uniaxial tensile BRS (along the x-direction) in samples milled at 0° (D3) and 90° (D12). The measured MIRS in sample D3 is the average of 3 measurements (Fig. 14). Far from the surface (> 0.25 mm), the data show the expected uniaxial tensile BRS along the milling direction ($\sigma_{\alpha\alpha}$ in D3) or the transverse direction ($\sigma_{\beta\beta}$ in D12) where the magnitudes are similar (100 MPa for D3 and 90 MPa for D12). Near the surface (< 0.10 mm) $\sigma_{\alpha\alpha}$ (Fig. 16(a)) is very similar in the two samples. The profile of $\sigma_{\alpha\beta}$ (Fig. 16(c)) is also very similar. There is a significant difference in the near surface (<

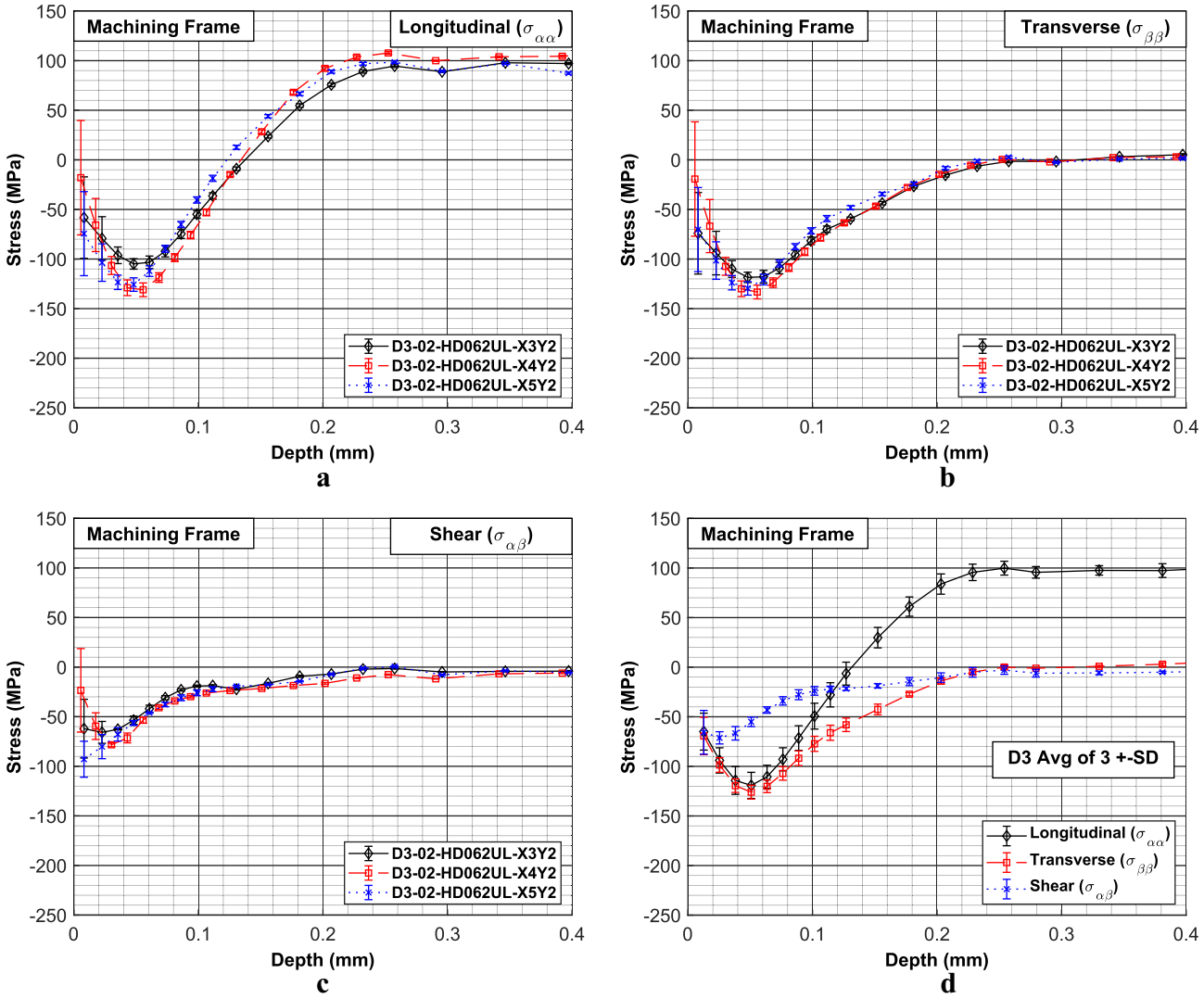

Fig. 14 Repeated MIRS data on sample D3 in region of tensile bulk residual stress for (**a**) longitudinal, (**b**) transverse, (**c**) shear stress and (**d**) the representative (average of three) depth profiles

0.10 mm) $\sigma_{\beta\beta}$, which has an elevation in peak compressive stress (-200 MPa) for tensile BRS along β. This magnitude is similar to that found for $\sigma_{\beta\beta}$ in 0° milling with compressive BRS along α (Fig. 15, D3 at X4Y1). Overall, the data (Fig. 16) show that the direction of BRS relative to the milling direction has a significant effect on MIRS.

Data assessment using elastic stress analysis

The right column of Fig. 9 shows distortion from the FE model in stress-relieved samples A20 milled at 0° (Fig. 9(b)) and B20 milled at 90° (Fig. 9(d)), and also in quenched sample D3 milled at 0°, where the wafer is removed in an area of near zero BRS (Fig. 9(f)). The computed distortion exhibits different peak to valley distortion (0.125, 0.08, and 0.16 mm for A20, B20, D3, respectively), but similar clocking angles (60° for A20, 56° for B20, and 60° for D3). The range of computed peak to valley distortion for the three samples is similar to the range of observed peak to valley distortion (compare the color ranges in the left column of Fig. 9 (observed)) to those in the right column (computed)). Overall, similarity of magnitude and clocking angle between computed and observed wafer distortion indicates consistency between measured MIRS and observed distortion.

The right column of Fig. 10 shows the computed distortion for wafers cut from quenched samples in areas of high BRS: sample D3 milled at 0° in areas of compressive (Fig. 10(b)) and tensile (Fig. 10(d)) BRS, and in sample D12 milled at 90° in an area of tensile BRS (Fig. 10(f)). FE model distortion was not computed in an area of

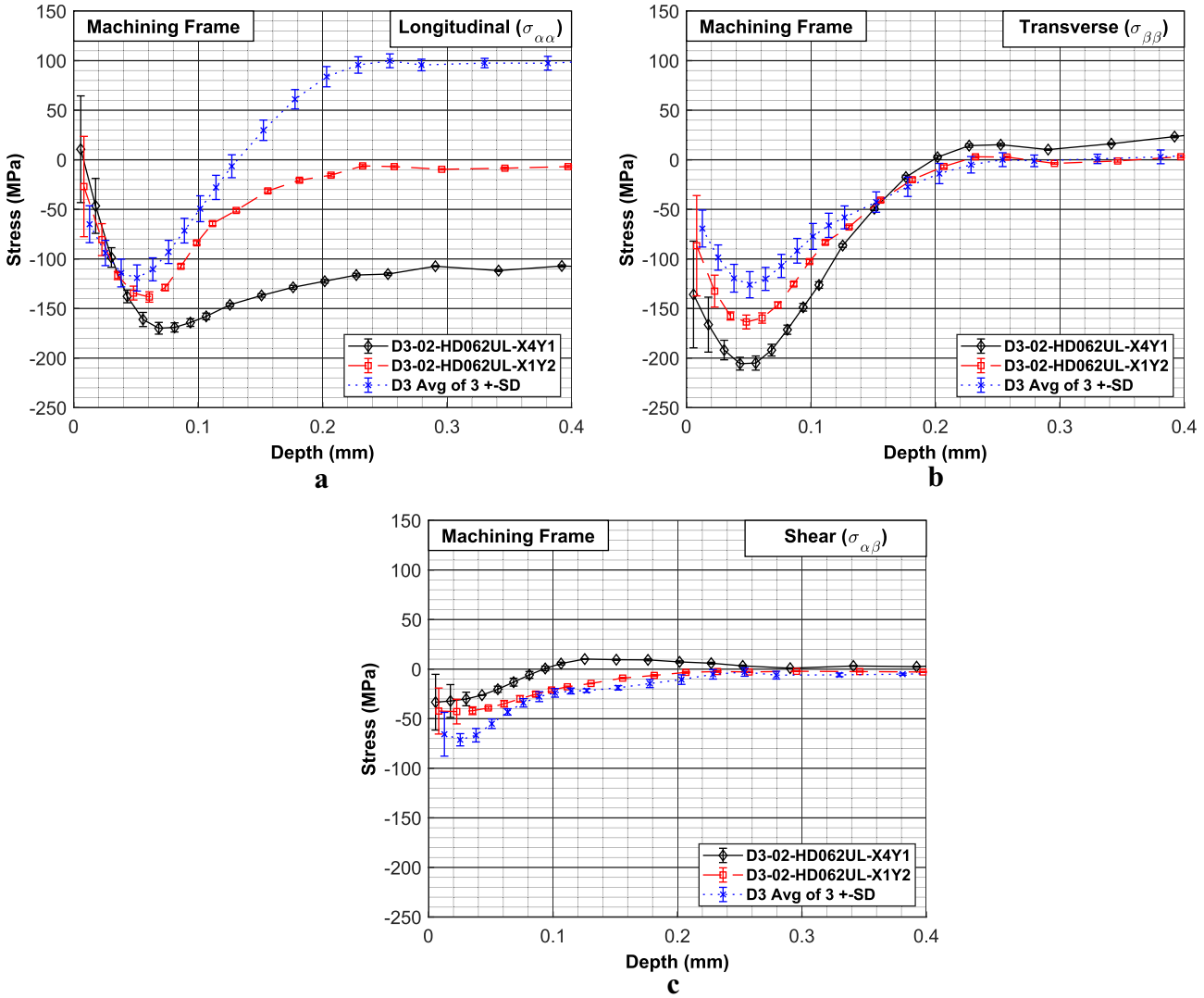

Fig. 15 MIRS data on sample D3 in regions of compressive (X4Y1), near zero (X1Y2), and tensile (average of 3) bulk residual stress for (**a**) longitudinal, (**b**) transverse, (**c**) shear components of stress.

compressive BRS for sample D12, milled at 90°. For sample D3, the computed peak distortion of the two wafers differ, being 0.15 mm in compressive BRS and 0.23 mm in tensile BRS. The clocking angles also differ, being 84° in compressive BRS and 28° in tensile BRS. Distortion of wafers cut from samples D3 and D12 in areas of tensile BRS, along α in D3 and along β in D12, exhibit very similar peak distortion of 0.23 mm but very different clocking angles of 28° in D3 and 71° in D12. Overall, computed distortions (right column of Fig. 10) are in good agreement with observed distortions (left column of Fig. 10) in both clocking angle and magnitude.

Figure 17 shows line plots of observed (left column Figs. 9 and 10) and computed (right column Figs. 9 and 10) distortion along θ_c. The general shapes of the measured and calculated distortions agree well from sample to sample with the largest differences occurring near the edges. There is good agreement for most cases, with the largest differences for stress-relieved sample B20 milled at 90° (Fig. 17(b)) and in sample D3 milled at 0° in tensile BRS (Fig. 17(e)).

Table 4 summarizes the SoM model parameters computed for samples A20, B20, D3 (for $\sigma_{\alpha\alpha} < 0$, $\sigma_{\alpha\alpha} \approx 0$, and $\sigma_{\alpha\alpha} > 0$), and D12 (for $\sigma_{\beta\beta} > 0$). The parameters comprise data determined from MIRS measurements including the bulk stress (σ_b), effective force components (F_{ij}), centroidal distances (h_{ij}), layer average principal stresses ($\tilde{\sigma}_1$ and $\tilde{\sigma}_2$), principal angle (θ_2), and bending moments ($\overline{M}_2$ and $\overline{M}_1$).

Values of bulk stress, σ_b, clearly show variation of the underlying BRS state (i.e., compressive, near zero, tensile) and are similar to those expected from the prior BRS measurements (Table 2, Figs. 2 and 3). The effective force from stress transverse to the milling direction $F_{\beta\beta}$ is consistently larger than or equal to the others, except in sample D3 milled in tensile BRS along α; the force from shear stress $F_{\alpha\beta}$ is smaller than the other forces and varies to a lesser degree across the range of BRS. The centroidal distances $h_{\alpha\alpha}$ and $h_{\beta\beta}$ are somewhat similar for each sample type. Across samples, magnitudes of $\tilde{\sigma}_2$ are consistently larger than those of $\tilde{\sigma}_1$, by convention, and values of θ_2 show significant variation with BRS that is particularly evident in the different wafer locations for sample D3. Subsequently, values of $\overline{M}_2$ are larger than values of $\overline{M}_1$, which is consistent with Eq. (7).

Table 5 summarizes data on the observed clocking angle, θ_c, and arc height, S_c, for all conditions, as well as data from the FE and SoM models; the data trends with BRS are presented in Figs. 18 and 19. The tabular data reinforce the trends in the surface topography discussed earlier. Clocking angles in low stress conditions (first four rows of the table) are similar for all wafers, with observed angles ranging from 45° to 50°, FE model angles ranging from 42° to 60°, and SOM model angles ranging from 41° to 60°. For the same sample, the two models provide consistent θ_c, being within 5° of one another for all samples except B20 (for which the difference is 14°); model angles are slightly larger than the

Fig. 17 Comparison of observed and computed (using FE model) distortions for low stress samples (**a**) A20 (0° milling), (**b**) B20 (90° milling), and high stress samples D3 (0° milling) in (**c**) compressive, (**d**) near zero, and (**e**) tensile BRS, and (**f**) D12 (90° milling) in tensile BRS. Reported values of BRS ($\sigma_{\alpha\alpha}$ and $\sigma_{\beta\beta}$) come from computed values of σ_b using hole-drilling data.

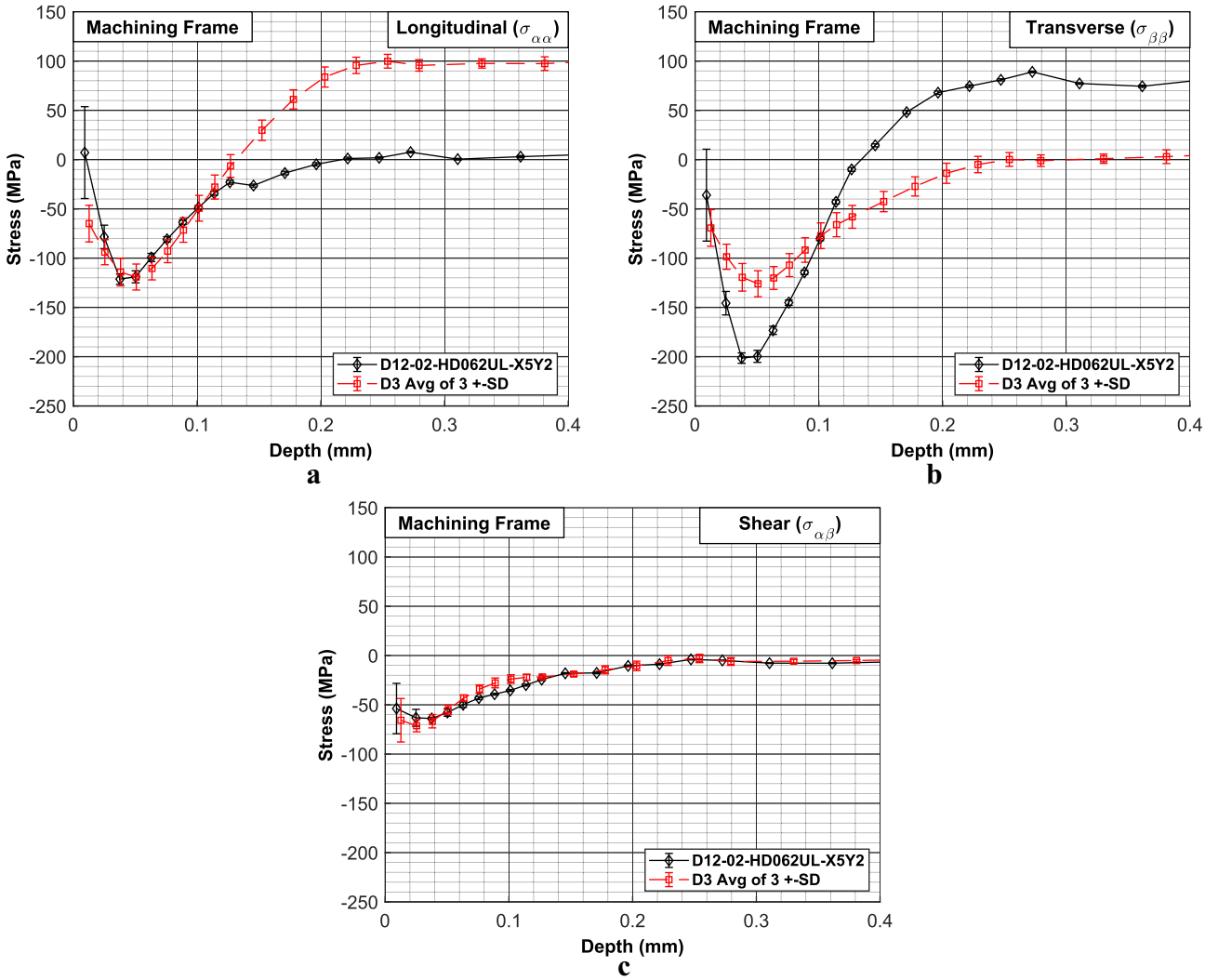

Fig. 16 MIRS data on high stress samples D3 (milling at 0°, along x) and D12 (milling at 90°, along y) in a region of tensile BRS

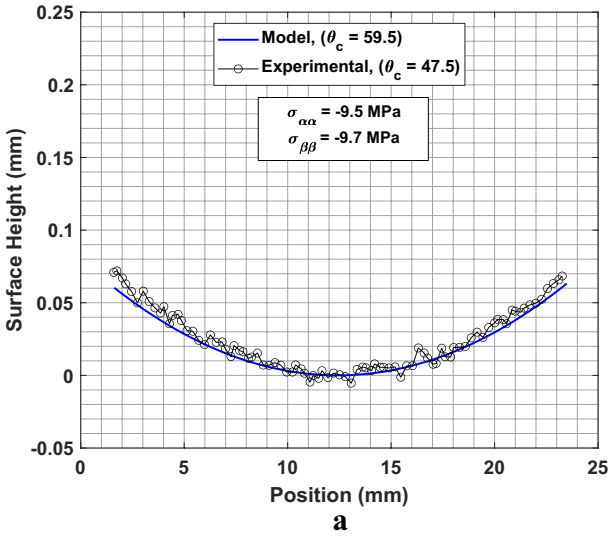
Model, (θ_c = 59.5)
Experimental, (θ_c = 47.5)
$\sigma_{\alpha\alpha}$ = -9.5 MPa
$\sigma_{\beta\beta}$ = -9.7 MPa
Surface Height (mm)
Position (mm)

a

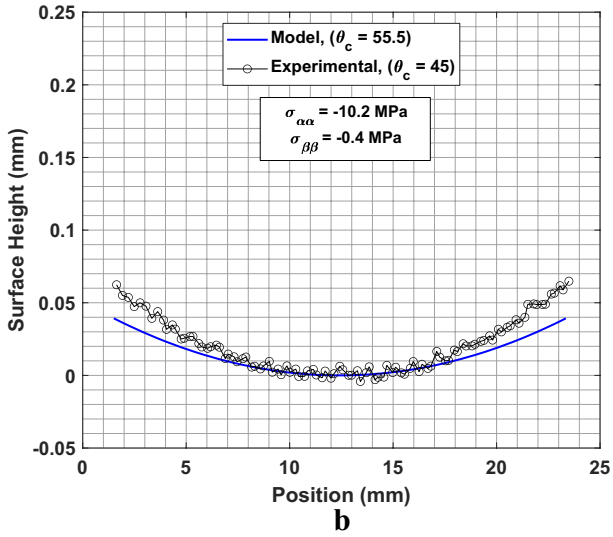
Model, (θ_c = 55.5)
Experimental, (θ_c = 45)
$\sigma_{\alpha\alpha}$ = -10.2 MPa
$\sigma_{\beta\beta}$ = -0.4 MPa
Surface Height (mm)
Position (mm)

b

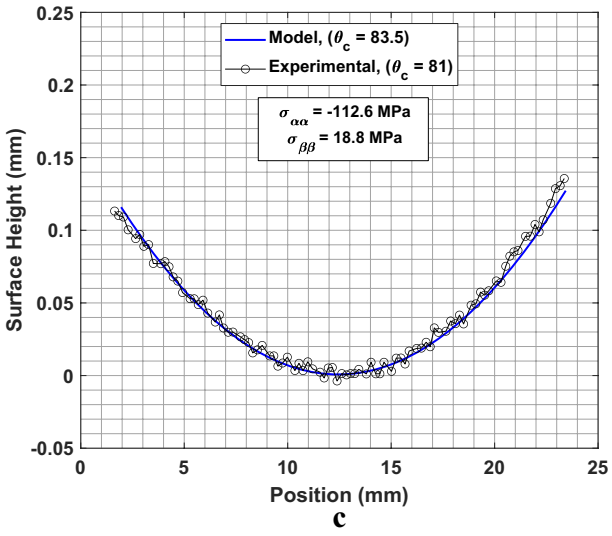
Model, (θ_c = 83.5)
Experimental, (θ_c = 81)
$\sigma_{\alpha\alpha}$ = -112.6 MPa
$\sigma_{\beta\beta}$ = 18.8 MPa
Surface Height (mm)
Position (mm)

c

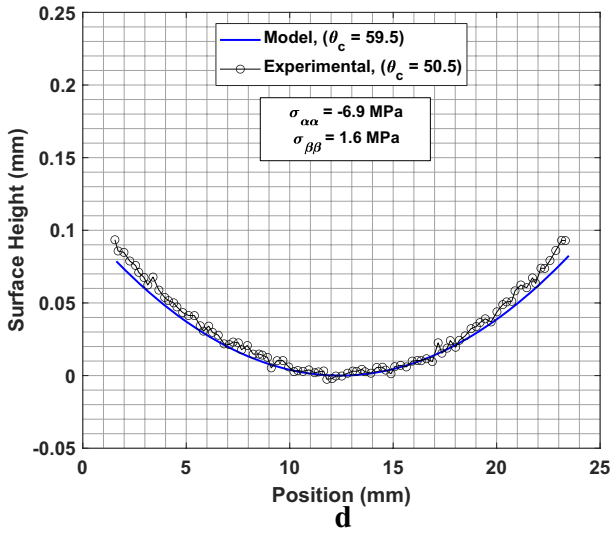
Model, (θ_c = 59.5)
Experimental, (θ_c = 50.5)
$\sigma_{\alpha\alpha}$ = -6.9 MPa
$\sigma_{\beta\beta}$ = 1.6 MPa
Surface Height (mm)
Position (mm)

d

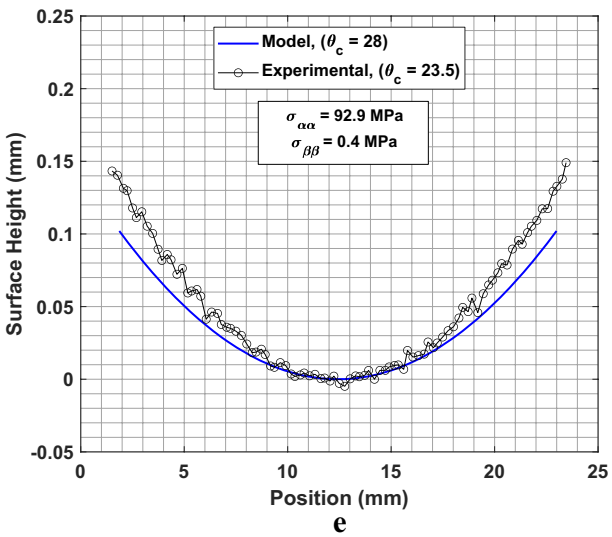
Model, (θ_c = 28)
Experimental, (θ_c = 23.5)
$\sigma_{\alpha\alpha}$ = 92.9 MPa
$\sigma_{\beta\beta}$ = 0.4 MPa
Surface Height (mm)
Position (mm)

e

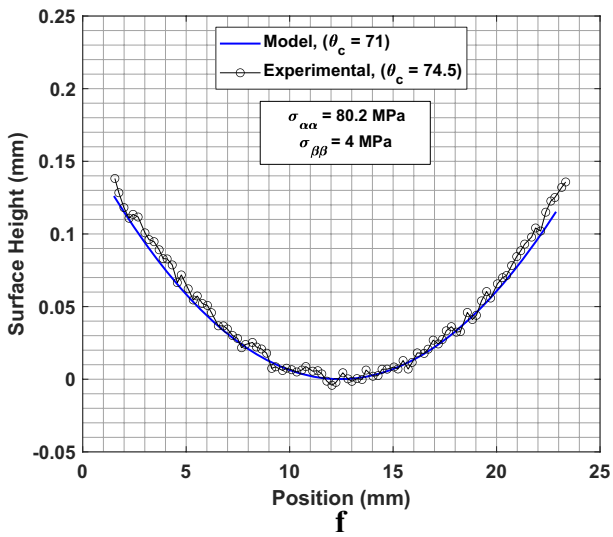
Model, (θ_c = 71)
Experimental, (θ_c = 74.5)
$\sigma_{\alpha\alpha}$ = 80.2 MPa
$\sigma_{\beta\beta}$ = 4 MPa
Surface Height (mm)
Position (mm)

f

Table 4 Summary of strength of materials model parameters. For samples A20 and B20 the results are computed using the average of three measurements. For sample B4 the results are computed using the average of six measurements

Sample ID	σ_b (MPa)	F_{ij} (N)	h_{ij} (mm)	$\overline{\sigma}_1$(MPa)	$\overline{\sigma}_2$(MPa)	θ_2(degrees)	$\overline{M}_2$(N•mm)	$\overline{M}_1$ (N•mm)
A20	$\sigma_{\alpha\alpha}$ = -9.5	$F_{\alpha\alpha}$ = -8.2	$h_{\alpha\alpha}$ = 0.081	-40.8	-88.1	60	-6.6	-2.7
	$\sigma_{\beta\beta}$ = -9.7	$F_{\beta\beta}$ = -11.9	$h_{\beta\beta}$ = 0.089					
	$\sigma_{\alpha\beta}$ = -4.9	$F_{\alpha\beta}$ = -3.2	$h_{\alpha\beta}$ = 0.064					
B4	$\sigma_{\alpha\alpha}$ = -11.8	$F_{\alpha\alpha}$ = -10.3	$h_{\alpha\alpha}$ = 0.061	-67.2	-128.5	54	-7.4	-3.6
	$\sigma_{\beta\beta}$ = -7.9	$F_{\beta\beta}$ = -12.4	$h_{\beta\beta}$ = 0.066					
	$\sigma_{\alpha\beta}$ = -5.0	$F_{\alpha\beta}$ = -3.4	$h_{\alpha\beta}$ = 0.047					
A18	$\sigma_{\alpha\alpha}$ = -10.8	$F_{\alpha\alpha}$ = -11.7	$h_{\alpha\alpha}$ = 0.068	-49.0	-109.7	44	-6.9	-2.9
	$\sigma_{\beta\beta}$ = -1.9	$F_{\beta\beta}$ = -11.4	$h_{\beta\beta}$ = 0.073					
	$\sigma_{\alpha\beta}$ = -6.0	$F_{\alpha\beta}$ = -4.4	$h_{\alpha\beta}$ = 0.077					
B20	$\sigma_{\alpha\alpha}$ = 0.4	$F_{\alpha\alpha}$ = -8.9	$h_{\alpha\alpha}$ = 0.065	-82.6	-136.7	42	-4.6	-4.7
	$\sigma_{\beta\beta}$ = -10.2	$F_{\beta\beta}$ = -8.9	$h_{\beta\beta}$ = 0.063					
	$\sigma_{\alpha\beta}$ = 1.5	$F_{\alpha\beta}$ = 0.0	$h_{\alpha\beta}$ = 0.033					
D3	$\sigma_{\alpha\alpha}$ = -6.9	$F_{\alpha\alpha}$ = -12.7	$h_{\alpha\alpha}$ = 0.079	-71.1	-208.8	62	-8.7	-4.7
	$\sigma_{\beta\beta}$ = 1.6	$F_{\beta\beta}$ = -18.1	$h_{\beta\beta}$ = 0.075					
	$\sigma_{\alpha\beta}$ = -2.1	$F_{\alpha\beta}$ = -4.0	$h_{\alpha\beta}$ = 0.069					
	$\sigma_{\alpha\alpha}$ = -112.6	$F_{\alpha\alpha}$ = -4.2	$h_{\alpha\alpha}$ = 0.081	-30.2	-191.4	85	-14.0	-2.0
	$\sigma_{\beta\beta}$ = 18.8	$F_{\beta\beta}$ = -27.2	$h_{\beta\beta}$ = 0.080					
	$\sigma_{\alpha\beta}$ = 4.5	$F_{\alpha\beta}$ = -2.2	$h_{\alpha\beta}$ = 0.036					
	$\sigma_{\alpha\alpha}$ = 92.9	$F_{\alpha\alpha}$ = -23.6	$h_{\alpha\alpha}$ = 0.070	-79.1	-191.4	25	-12.7	-4.7
	$\sigma_{\beta\beta}$ = 0.4	$F_{\beta\beta}$ = -13.8	$h_{\beta\beta}$ = 0.077					
	$\sigma_{\alpha\beta}$ = -4.1	$F_{\alpha\beta}$ = -6.0	$h_{\alpha\beta}$ = 0.060					
D12	$\sigma_{\alpha\alpha}$ = 4.0	$F_{\alpha\alpha}$ = -10.6	$h_{\alpha\alpha}$ = 0.078	-60.4	-200.2	73	-12.2	-4.0
	$\sigma_{\beta\beta}$ = 80.2	$F_{\beta\beta}$ = -27.6	$h_{\beta\beta}$ = 0.072					
	$\sigma_{\alpha\beta}$ = -6.1	$F_{\alpha\beta}$ = -5.7	$h_{\alpha\beta}$ = 0.070					

observed angles. Arc heights in low stress conditions are also similar, with observed arc heights ranging from 0.052 to 0.076 mm, FE model arc heights ranging from 0.033 to 0.063 mm, and SOM arc heights ranging from 0.026 to 0.052 mm. Arc heights from the two models are mostly similar for each low stress sample, being within 0.008 mm, except for sample B20 which differs by 0.011 mm; for all wafers, arc heights from both models are smaller than arc heights observed.

There are clear trends in θ_c and S_c for variation of σ_b in the quenched samples that are apparent in the last five rows of Table 5 and in Figs. 18 and 19. For clocking angle, data from sample D3 milled at 0° show a linear trend of decreasing θ_c with increasing BRS along α (Fig. 18). As BRS along α changes from -112.6 to -6.9 to 92.9 MPa, the data follow a linear trend in θ_c for observed data (80° to 51° to 22°), the FE model (84° to 60° to 28°), and the SoM model (85° to 62° to 25°). Clocking angle data from samples B20 and D12 milled at 90° show a different linear trend, where θ_c increases with decreasing BRS along β (Fig. 18). As BRS along β changes from 80.2 to -10.2 to -76 MPa, the trend in θ_c is consistent for observed data (13.5 to 45° to 74°), the FE model (56° to 71°) and the SOM model (42° to 73°). Model results were not computed for sample D12 milled at 90°, as stated above. The differing trend of θ_c with BRS in each direction is distinctive. For arc height, data from sample D3 milled at 0° show a parabolic trend of S_c with BRS along α (Fig. 19). As BRS along α increases from -112.6 to -6.9 to 92.9 MPa, the parabolic trend is consistent for observed data (0.106 to 0.077 to 0.121 mm), the FE model (0.105 to 0.067 to 0.091 mm), and the SoM model (0.113 to 0.060 to 0.094 mm). Arc height for sample B20 and D12 milled at 90° show that as BRS along β increases from -76 to -10.2 to 80.2 MPa the parabolic trend is consistent for observed data (0.079 to 0.052 to 0.114 mm), the FE model (0.033 to 0.106 mm), and the SoM model (0.026 to 0.091 mm). Overall, the S_c data suggest that distortion magnitude depends on BRS magnitude, and not BRS sign or direction, while the θ_c data

Table 5 Summary of bulk residual stress from hole-drilling along with clocking angle (θ_c) and peak arc height (S_c) computed from observed wafer topography, FE models, and SoM model. For samples A20 and B20 the observed results are for an average of three wafers

Sample ID	Milling Direction	σ_b (MPa)	Observed		FE Model		SoM Model	
			θ_c	S_c (mm)	θ_c	S_c (mm)	θ_c	S_c (mm)
A20	0°	$\sigma_{\alpha\alpha}$ = -9.5 $\sigma_{\beta\beta}$ = -9.7 $\sigma_{\alpha\beta}$ = -4.9	50°	0.059	60°	0.052	60°	0.048
B4	0°	$\sigma_{\alpha\alpha}$ = -11.8 $\sigma_{\beta\beta}$ = -7.9 $\sigma_{\alpha\beta}$ = -5.0	49°	0.076	50°	0.063	54°	0.052
A18	0°	$\sigma_{\alpha\alpha}$ = -10.8 $\sigma_{\beta\beta}$ = -1.9 $\sigma_{\alpha\beta}$ = -6.0	-	-	41°	0.058	44°	0.050
B20	90°	$\sigma_{\alpha\alpha}$ = 0.4 $\sigma_{\beta\beta}$ = -10.2 $\sigma_{\alpha\beta}$ = 1.5	45°	0.052	56°	0.033	42°	0.026
D3	0°	$\sigma_{\alpha\alpha}$ = -6.9 $\sigma_{\beta\beta}$ = 1.6 $\sigma_{\alpha\beta}$ = -2.1	51°	0.077	60°	0.067	62°	0.060
		$\sigma_{\alpha\alpha}$ = -112.6 $\sigma_{\beta\beta}$ = 18.8 $\sigma_{\alpha\beta}$ = 4.5	80°	0.106	84°	0.105	85°	0.113
		$\sigma_{\alpha\alpha}$ = 92.9 $\sigma_{\beta\beta}$ = 0.4 $\sigma_{\alpha\beta}$ = -4.1	22°	0.121	28°	0.091	25°	0.094
D12	90°	$\sigma_{\alpha\alpha}$ = 4.0 $\sigma_{\beta\beta}$ = 80.2 $\sigma_{\alpha\beta}$ = -6.1	74°	0.114	71°	0.106	73°	0.091
		$\sigma_{\alpha\alpha}$ = 9.4 $\sigma_{\beta\beta}$ = -76 $\sigma_{\alpha\beta}$ = -10.4	13.5°	0.079	-	-	-	-

show that the sign and direction of BRS affect the orientation of the distortion. The data also show that the models, based on residual stress measurements, are useful in tying measured residual stress to observed distortion.

Discussion

Methodological issues

The approach to sample preparation was useful in supporting the objectives of this study. A set of samples with consistent residual stress resulted from cutting plates near the mid-length of larger blocks that had been uniformly heated and then quenched (see Fig. 1). The quenching step created a BRS field with large magnitude (100 MPa to -150 MPa) and distinct regions of nearly uniaxial residual stress (Figs. 2 and 3). These distinct regions enabled the study of the interaction between BRS and MIRS in samples with high BRS. Stress-relieved samples provided a useful complement to the quenched samples, enabling determination of MIRS in conditions of negligible BRS (< 15 MPa). The measurements of BRS made using slitting (Table 3) agree with bulk stress σ_b determined from hole-drilling data at specific locations (Table 4). Stress-relieved samples have σ_b less than ±10 MPa (Table 4), and quenched samples exhibit nearly uniaxial σ_b that varies from high compression (-113 MPa) to high tension (93 MPa). These BRS levels agree with those found in prior work on residual stress in 7050T74 and 7050T7451 [16].

The wafer distortion experiment provides a practical method to assess and visualize the distortion induced by milling (or other types of machining), as first noted in our recent related work [5]. The 1 mm wafer thickness was selected as being significantly larger than the depth of the milling induced residual stress field (ranging from about 0.10 to 0.25 mm) but small enough to provide a distorted surface form that is readily measured using a typical profilometer (roughly 0.25 mm peak to valley); a smaller or larger wafer thickness might be useful in other work. In manufacturing applications, where part thickness is often

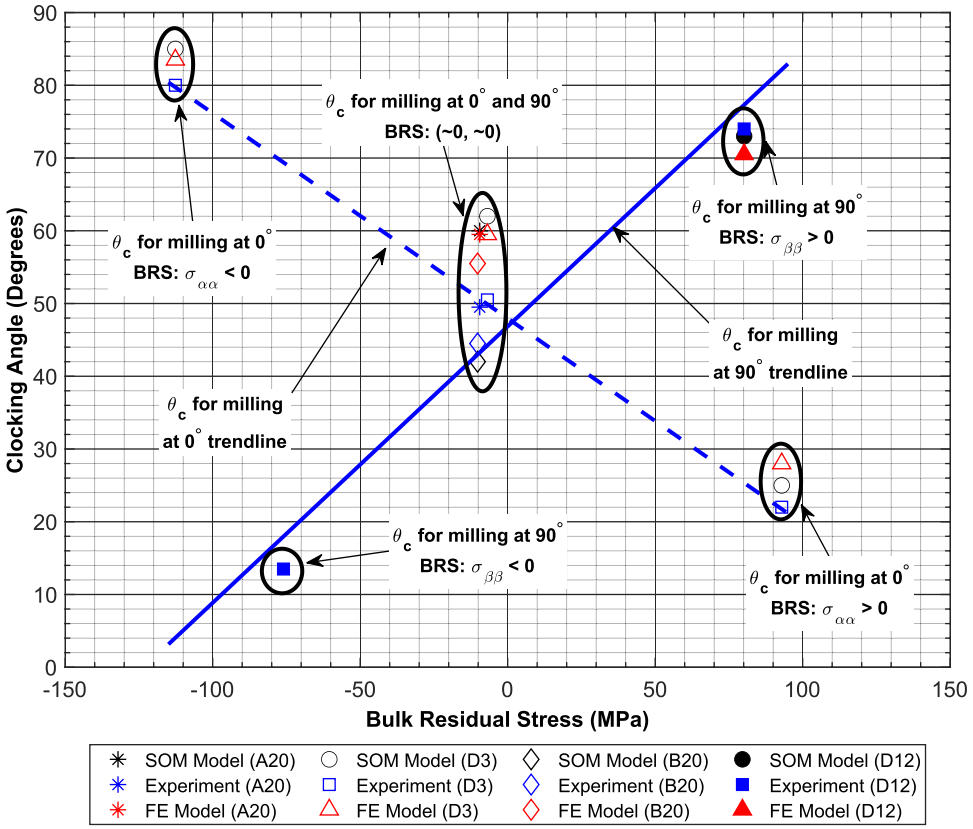

Fig. 18 Plot of θ_c versus BRS from wafer experiment, FE model, and SoM model data

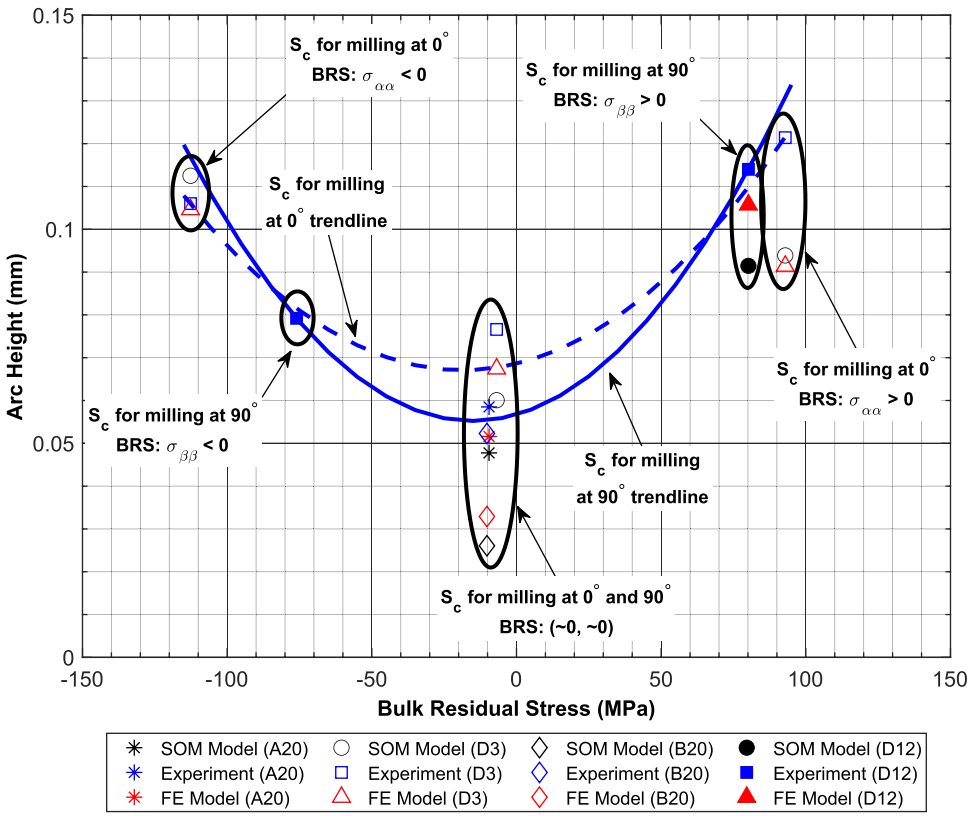

Fig. 19 Plot of S_c versus BRS from wafer experiment, FE model, and SoM model data

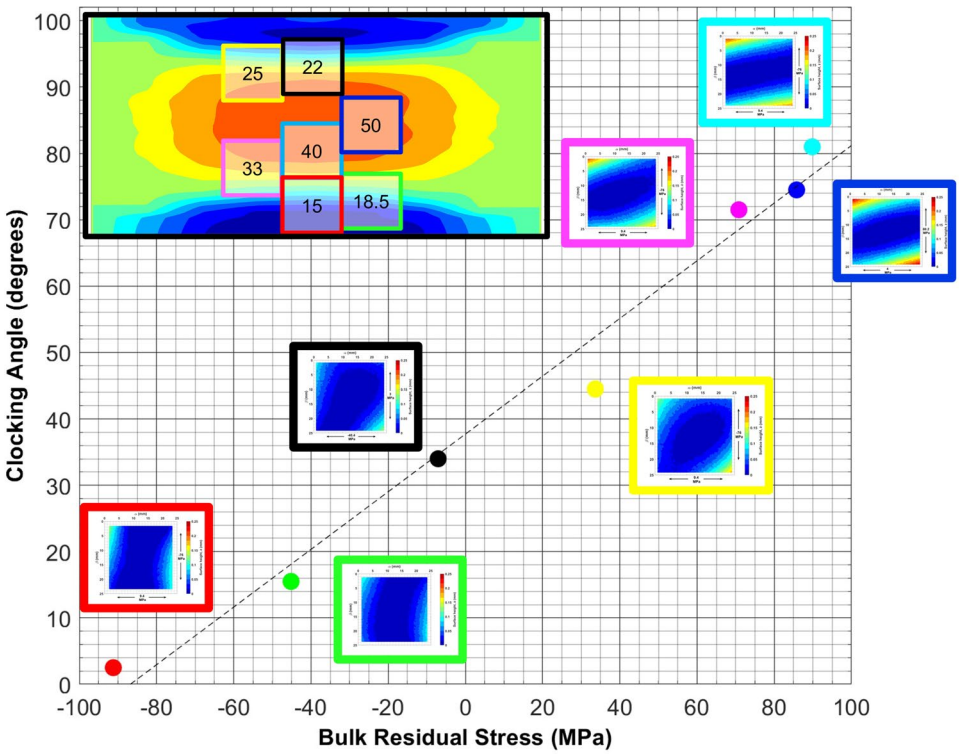

Fig. 20 Effect of BRS on clocking angle for seven wafers removed from sample D12 milled at 90; inset at upper left shows locations of wafer removals superposed on color map of BRS along plate length (σ_{xx}) with numerical values indicating distance (mm) from wafer center to nearest sample edgere

larger (e.g., 2 to 6 mm or more), peak-to-valley distortion would be smaller than that observed in the wafer, with the radius of curvature scaling approximately with the square of thickness (as shown by Eqs. (8) and (9) for $t_w \gg h$).

Replicate wafer experiments performed in stress-relieved sample B20 show that observed wafer distortion is repeatable (Fig. 8). Beyond the similarities in Fig. 8, data analysis for the three wafers reveals consistent magnitudes of arc height ($S_c = 0.053$, 0.055, and 0.061 mm with an average of 0.056 mm (similar to the value obtained from the three-wafer average topography data reported in Table 5, 0.052 mm)), and clocking angle ($\theta_c = 47°$, 47°, and 38° with an average of 45° (similar to the value reported in Table 5, 45°)). Differences between wafer distortions could be attributed to variations in the processes of wafer removal and surface form measurement or to spatial variations of material condition and/or milling.

The companion stress analysis models, based on SoM and FE techniques, connect and complement the wafer distortion and MIRS experiments. Because the models use as input the measured MIRS depth profiles, their output converts measured MIRS to expected distortion. The satisfactory comparisons between computed and observed distortion fields (compare left and right columns of Figs. 9 and 10) and analytical distortion metrics (Table 5) bring confidence to the trends established between distortion and BRS (Figs. 18 and 19). Comparing the models, we note that the FE model has fewer assumptions, requires little processing of the input MIRS profiles, and provides a two-dimensional distortion field output; on the other hand, the SoM model uses simple, closed form calculations and produces output distortion metrics (θ_c and S_c) that have a similar degree of agreement with the observed metrics as do the metrics derived from the FE model (Table 5). Either model could be useful for further work.

Significance and interpretation of results

Hole-drilling data from three replicate stress-relieved samples milled in the same way show that the three samples have similar but somewhat different MIRS profiles (Fig. 12). The dispersion of the average MIRS depth profile from sample to sample is significantly larger than the dispersion of single MIRS depth profiles in a single sample (compare Figs. 11 and 12). Expected causes for this dispersion are variations in material, heat treatment, tool condition (e.g., tool wear), or milling condition. Because the present samples were taken from a single plate with uniform heat treatment, it is unlikely the MIRS differences are due to variations in material or heat treatment. A more detailed follow-on study could address this question in more detail, with specific attention to milling conditions.

Distortion of wafers removed from locations with different BRS show clear differences (see left column of Figs. 9 and 10), with a notable rotation of the principal directions of curvature relative to the milling direction. The rotation

of the principal directions of curvature is indicated by θ_c which changes with the direction, magnitude, and sign of BRS relative to the milling direction. The dependence of θ_c on BRS found in the wafer distortion experiments should also be found in milling-induced distortion observed in part manufacture; a distortion model accounting for this effect would be useful but is presently lacking.

Since wafers removed from locations with different BRS show trends in clocking angle with BRS, multiple wafers were removed from high stress sample D12 milled at 90° to confirm the linear trend of Fig. 18. Values of BRS are taken from the prior CMOD slitting measurements (Fig. 2), which gives stress as a function of position within the sample. Wafers are then removed at 7 different locations (shown superposed on the stress map in Fig. 20). Wafer surface form data confirm that BRS trends linearly with clocking angle. In this sample milled at 90°, the BRS is nearly uniaxial along β (transverse to the milling direction) and the trend is increasing BRS correlated to increasing clocking angle. On the other hand, samples milled at 0° show an opposite linear trend, with increasing BRS correlated to decreasing clocking angle (Fig. 18).

The influence of BRS on milling induced distortion appears phenomenologically consistent with the influence of preloading on distortion achieved in shot peen forming (SPF). In SPF a preload is commonly applied (e.g., bending along a specific direction and tension on the peened surface) with the intent to increase curvature along the direction of tension (e.g., [17]). Forming a part without preload produces spherical curvature while SPF with tensile preload produces cylindrical curvature of smaller radius along the direction of the tensile preload. The greater curvature occurs because the material flows more readily in the direction of tensile preload during the shot peening process.

The trend in SPF is analogous to what occurs during milling, where the BRS field (see Figs. 2 and 3) acts as a preload. Considering data from sample D3, when the level of BRS along α is near zero (no preloading present) milling along α produces an elliptical curvature with $\theta_c = 51°$. As the magnitude of BRS along α increases (preloading is present) milling along α produces elliptical curvature rotated further from, or closer to, the milling direction depending on the sign of BRS. When the BRS along α is tensile the material flows more in the direction of the tension, rotating the curvature closer to the milling direction ($\theta_c = 22°$). When BRS along α is compressive the opposite occurs: the curvature rotates away from the milling direction ($\theta_c = 80°$). When the BRS along β is tensile, as for sample D12, the clocking angle ($\theta_c = 74°$) is similar to that observed when BRS is compressive along α ($\theta_c = 80°$). When the BRS along β is compressive the clocking angle ($\theta_c = 13.5°$) is similar to that observed when BRS is tensile along α ($\theta_c = 22°$). Overall, the effects of BRS on distortion and curvature are similar to the effects of preloading in SPF, depending on BRS sign and magnitude, and the relative directions of BRS and milling.

Conclusion

This paper assessed interactions between bulk residual stress and milling induced residual stress and their effects on distortion in milled aluminum. This was accomplished by producing sets of identically prepared samples having high or low bulk residual stress, milling them, and performing fine-increment hole-drilling residual stress measurements and wafer distortion experiments. The hole-drilling data show that bulk residual stress has a significant effect on residual stress induced by milling. The wafer distortion data show that combinations of bulk and milling induced residual stress lead to significant differences in distortion. The measured residual stresses are used further, in two different elastic stress analysis models, one based on finite element methods and one based on strength of materials theory (plate bending). The models output distortions with similar curvature and clocking, with both model outputs being similar to observed wafer distortion, showing that the measured residual stress and observed distortions are consistent with one another.

A principal effect of bulk residual stress on milling induced distortion is to rotate the principal axes of curvature, quantified by the clocking angle, relative to the milling tool travel direction. Samples milled with low magnitude bulk residual stress (< 10 MPa) created an elliptical curvature clocked at a characteristic angle between 44° and 48° relative to the milling direction. Samples milled with high magnitude bulk residual stress along the milling direction exhibit a changed clocking angle, which is rotated toward or away from the milling direction depending on the sign of the bulk residual stress. A second effect of bulk residual stress on milling induced distortion is to increase the amount distortion. The distortions (peak arc height) found in samples milled with high magnitude bulk residual stress are nearly double those found in samples with low magnitude bulk residual stress.

Acknowledgements This work was performed in the context of a collaborative project between the University of California, Davis (UC Davis) and the Technische Universität Kaiserslautern (TUK). UC Davis received funding from the National Science Foundation under Award No. 1663341 (Division of Civil, Mechanical and Manufacturing Innovation (CMMI)). Any opinions, findings, and conclusions or recommendations expressed in this material are those of the authors and do not necessarily reflect the views of the National Science Foundation. TUK received financial support from Deutsche Forschungsgemeinshaft (DFG) under project AU 185/64-1 (351381681).

Declarations

Conflict of interest This study was performed by the authors with the support noted above. No authors report any potential conflict of interest that played a significant role in the work reported.

References

1. Li J, Wang S (2017) Distortion caused by residual stresses in machining aeronautical aluminum alloy parts: recent advance. Int J Adv Manuf Tachnol. 89:997–1012. https://doi.org/10.1007/s00170-016-9066-6
2. Olson MD, Hill MR (2018) Two-dimensional mapping of in-plane residual stress with slitting. Exp Mech 58:151–166. https://doi.org/10.1007/s11340-017-0330-y
3. Masoudi S, Amini S, Saeidi E, Eslami-Chalander H (2015) Effect of machining-induced residual stress on the distortion of thin-walled parts. Int J Adv Manuf Technol. 76:597–608. https://doi.org/10.1007/s00170-014-6281-x
4. Madariaga A, Perez I, Arrazola PJ, Sanchez R, Ruiz JJ, Rubio FJ (2018) Reduction of distortions in large aluminum parts by controlling machining-induced residual stresses. Int J Adv Manuf Technol. 97:967–978. https://doi.org/10.1007/s00170-018-1965-2
5. Chighizola CR, D'Elia CR, Weber D, Kirsch B, Aurich JC, Linke BS, Hill MR (2021) Intermethod comparison and evaluation of measured near surface residual stress in milled aluminum. Exp Mech 61:1309–1322. https://doi.org/10.1007/s11340-021-00734-5
6. Prime MB, DeWald AT (2013) The Contour Method. In: Schajer GS (ed) Practical Residual Stress Measurement Methods. Wiley, United Kingdom, pp 109–138
7. Zhang Z, Li L, Yang Y, He N, Zhao W (2014) Machining distortion minimization for the manufacturing of aeronautical structure. Int J Adv Manu Technol. 73:1765–1773. https://doi.org/10.1007/s00170-014-5994-1
8. Handbook ASM (1991) Heat Treating of Aluminum Alloys. ASM Handbook. 4:841–879. https://doi.org/10.1361/asmhba0001205
9. Tang ZT, Liu ZQ, Wan Y, Ai X (2008) Study on Residual Stresses in Milling Aluminium Alloy 7050-T7451. In: Yan XT., Jiang C., Eynard B. (eds) Advanced Design and Manufacture to Gain a Competitive Edge. Springer, London. https://doi.org/10.1007/978-1-84800-241-8_18
10. Weber D, Kirsch B, Chighizola CR et al (2021) Analysis of machining-induced residual stresses of milled aluminum workpieces, their repeatability, and their resulting distortion. Int J Adv Manuf Technol 115:1089–1110. https://doi.org/10.1007/s00170-021-07171-7
11. Chighizola CR, Hill MR (2020) Mapping of bulk residual stress using cut mouth opening displacement, submitted for publication to experimental mechanics. https://doi.org/10.1007/s11340-021-00745-2
12. ASTM E837–13a (2013) Standard test method for determining residual stresses by the hole-drilling strain-gage method. Testing Standard, West Conshohocken, PA: ASTM International. https://doi.org/10.1520/E0837-13A
13. Grant P, Lord J, Whitehead P, Fry AT (2006) The application of fine increment hole drilling for measuring machining-induced residual stresses. Applied Mechanics and Materials. 3–4:105–110. https://doi.org/10.4028/www.scientific.net/AMM.3-4.105
14. ABAQUS/Standard, Version 6.14. (2014) Dassault Systems, Simulia Corporation.
15. Weisstein EW. Circular Segment. From MathWorld--A Wolfram Web Resource. https://mathworld.wolfram.com/CircularSegment.html
16. Prime MB, Hill MR (2002) Residual stress, stress relief, and inhomogeneity in aluminum plate. Scr Mater 46(1):77–82. https://doi.org/10.1016/51359-6462(01)01201-5
17. Faucheux PA, Gosselin FP, Lévesque M (2018) Simulating shot peen forming with eigenstrains. J Mater Process Technol 254:135–144. https://doi.org/10.1016/j.jmatprotec.2017.11.036